International Journal of Sustainable Aviation

ISSN online: 2050-0475 - ISSN print: 2050-0467
https://www.inderscience.com/ijsa

The role of pressure field dynamics on the onset of transonic aeroelastic instabilities of high aspect ratio swept wings

Mario Rosario Chiarelli, Salvatore Bonomo

DOI: 10.1504/IJSA.2023.10057434

Article History:

Received:	17 January 2023
Last revised:	30 April 2023
Accepted:	11 May 2023
Published online:	18 October 2023

The role of pressure field dynamics on the onset of transonic aeroelastic instabilities of high aspect ratio swept wings

Mario Rosario Chiarelli* and
Salvatore Bonomo

Department of Civil and Industrial Engineering,
University of Pisa,
Largo Lucio Lazzarino 1, 56122
Pisa, Italy
Email: mario.rosario.chiarelli@unipi.it
Email: salvatore.bonomo.79@gmail.com
*Corresponding author

Abstract: The dynamic aeroelastic responses in the transonic regime for a conventional swept wing and a curved-planform wing, both having a high aspect ratio, are analysed in detail. Using 2-way fluid structure interaction (FSI) analysis, the power spectral density of both wing-tip displacements and wing aerodynamic coefficients are analysed to highlight instabilities. Furthermore, a study of the interaction between the structural dynamics and the dynamics of the pressure field is performed. To do this, transient computational fluid dynamics (CFD) analyses, performed on rigid wings with updated geometry, provided the frequency spectra of the pressure fields. For the conventional swept wing, a clear interaction between a structural bending mode and pressure field oscillations generates a flutter-buffet instability. Conversely, for the curved-planform wing, this work demonstrated that the transonic pressure field oscillations, although not negligible, are not a direct cause of the onset of the bending-torsion flutter of the wing.

Keywords: swept wing; curved-planform wing; onset of transonic aeroelastic instabilities; flutter-buffet; bending-torsion flutter; FSI analyses; CFD analyses; pressure field dynamics.

Reference to this paper should be made as follows: Chiarelli, M.R. and Bonomo, S. (2023) 'The role of pressure field dynamics on the onset of transonic aeroelastic instabilities of high aspect ratio swept wings', *Int. J. Sustainable Aviation*, Vol. 9, No. 4, pp.332–370.

Biographical notes: Mario Rosario Chiarelli is an Associate Professor in the field of Aerospace Structures at the University of Pisa since 2001. His research activities concern fracture mechanics, fatigue of metallic materials, structural buckling, and aeroelasticity.

Salvatore Bonomo has a Master's degree in Aerospace Engineering from the University of Pisa. His master thesis concerned the use of FSI techniques to analyse the aeroelastic behaviour of high aspect ratio wings. He is currently working as an R&D Design Engineer at INFIBRA TECHNOLOGIES Srl in Pisa.

This paper is a revised and expanded version of a paper entitled 'Role of the pressure field harmonic oscillations in the flutter and flutter-buffet phenomena of high aspect ratio swept wings' presented at International Symposium on Aircraft Technology, MRO and Operations, Belgrade, Serbia, 14–16 September 2022.

1 Introduction

1.1 Motivation and literature review

To increase the efficiency of modern aircrafts the wings are designed to reduce the drag and structural weight; however, it is well known that highly flexible wing structures can undergo undesirable aeroelastic phenomena due to aerodynamic force oscillations that can occur at the onset of high-speed buffet. High aspect ratio wings, due to their high flexibility, are therefore very sensitive to the aerodynamic loads that develop at high speed and/or high Mach number. In the transonic buffet region, the shock waves on the aircraft wings tend to oscillate and, consequently, the separation of the boundary layer amplifies the pressure variations on the wing surfaces. In order to ensure both structural integrity and safety, regarding the flight envelope of an aircraft, for a fixed weight and a desired Mach number, a maximum cruising flight altitude is defined: this altitude allows for a sufficient buffet margin for manoeuvring and for any gust conditions.

According to a proposed and partially validated theory presented in Lee (2001), Xiao et al. (2006), Hartmann et al. (2012), Feldhusen-Hoffmann et al. (2018), and Petrocchi et al. (2022) under particular physical conditions, the propagation of sound pressure waves that beat upward at the sonic zone boundaries causes fore and aft movements of these boundaries: i.e., the shock waves oscillations. For this reason, the pressure field that develops around a wing, in terms of spatial distribution and frequency content, affects the stability of a transonic flow.

Numerical and/or experimental results present in the literature show a well-defined periodicity of the physical quantities observed in buffet conditions. LCOs occur due to the effect of a fundamental frequency and its super harmonics: see Xiong et al. (2012), Gao et al. (2015), Zhang et al. (2015), Gao et al. (2016), Giannelis et al. (2017), Iovnovich et al. (2015), Sartor and Timme (2015), Sartor and Timme (2016), Sartor and Timme (2017). In the transonic regime, the periodicity is more pronounced approaching the onset of the buffet condition (pre-buffet condition), that is, in a condition for which the perturbations in the aerodynamic field are very small, as highlighted in Sartor and Timme (2015).

When a buffet condition is established, a period-1 LCO often characterises lift and/or pressure oscillations: i.e., in general, the fundamental frequency of the oscillations in the flow field drives the response of the system, see Gao and Zhang (2020) and Gao et al. (2021).

Almost all of the literature investigating three-dimensional buffet conditions refers to rigid models. In other words, the deformed shape of the lifting surfaces is not considered.

However, buffet conditions are very sensitive to changes in the angle of attack, as several two-dimensional and three-dimensional results demonstrate. For this reason, the deformed shape of a wing, which depends on the trim conditions and which can change

with the onset of dynamic instability, plays a very important role and it cannot be ignored when the unstable conditions of a transonic flow need to be identified.

For a three-dimensional situation, e.g. a swept wing with a sweep angle greater than 20°, Iovnovich et al. (2015) shows how unstable flows that involve the whole span of the wing, originate at the root section where positive and negative pressure fluctuations are generated periodically. A *lateral flow mode* appears, in which, repeated *buffet cells* propagate in the span wise direction.

Similar conclusions can be found in Plante et al. (2017) where for the examined flow conditions, *buffet cells* (i.e., specific flow structures) appear along the span. While these cells appear to be uncorrelated for low sweep angles, the results suggest a span wise organisation and convection of those cells towards the tip of the wing with increasing sweep angles.

Due to the span wise effects, Plante et al. (2017) show that the frequency of a three-dimensional buffet is correlated to the wavelength of these cells. In addition, from a technical point of view, computations on a coarser grid and with multiple turbulence models show that the URANS model robustly predicts the downstream shock position.

Similarly, in Sartor and Timme (2017) shock instability occurs on time scales much longer than those of wall-bounded turbulence, i.e., boundary layer physics is not directly involved in the onset of transonic instability phenomena. From a numerical point of view, the results in Sartor and Timme (2016) indicate that an unsteady RANS approach is able to describe the main features of the buffet phenomenon. Similar remark is also expressed in Gao and Zhang (2020): "*the URANS method is suitable for the simulation of transonic unsteady problems, i.e., transonic buffet flow*". Moreover, the literature review shows that, for this type of analysis, it is not necessary for the grids to represent very precisely the boundary layer around the wing surface. These last indications represented a reference for carrying out the numerical activities of our research.

1.2 Summary of previous results and introduction to the new data analysis

As mentioned in Chiarelli and Bonomo (2016, 2019) to perform the CFD analyses we used the unsteady RANS methodology implemented in ANSYS Inc. (2013) with coarse grids. Aerodynamic grids of about 400,000 hexahedral cells and 400,000 nodes were used to carry out both rigid and 2-way FSI analyses on swept and curved-wing models. A sensitivity analysis, discussed in detail in Chiarelli and Bonomo (2019), shows that for 'coarse' grids the expected errors on lift coefficients are less than 10% and the expected errors on drag coefficients are approximately 25%. The wing models analysed have the same span, the same aspect ratio, the same profiles, the same chords, the same reference surface, and the same angle of sweep at the leading edge of the root section. Only their planforms are different. The structural material is an aluminium alloy. The total mass of each model was approximately 45,400 kg (including engine mass). Structured grids implement both aerodynamic wing models; they have the same number of cells and the same cell size, so similar numerical errors affect both models. Therefore, the comparison of the aeroelasticity of the wings and the comparison of the respective aerodynamic fields are based on the use of numerical models with similar characteristics (same topology of aerodynamic grid, same number and distribution of cells and nodes, etc.). Table 1 summarises the geometric characteristics of the two wings. The planform shape of the swept wing follows, albeit in first approximation, that of the wing of the B787 transport aircraft, while the profile used is the 10% Thick Supercritical Airfoil SC(2)-0410 as

illustrated in Chiarelli et al. (2010). The geometry of the curved wing was obtained by shifting the section profiles of the swept wing in the stream-wise direction (sheared wing) following a predetermined shape of the leading edge, from kink section to tip section. The detailed description of this methodology is described in Chiarelli and Bonomo (2016).

Table 1 Geometric features of the two half-wing models

	Swept wing	*Curved wing*
Aspect ratio	9.5	9.5
Angle of sweep at root	32º	32º
Angle of sweep at tip	32º	53º
Half-wing span	30 m	30 m
Reference surface area	379 m^2	379 m^2
Root chord	13.18 m	13.18 m
Tip chord	1.7 m	1.7 m
Kink section position	9.3 m	9.3 m
Kink chord	7.37 m	7.37
Dihedral angle	5º	5º

Figure 1 and Figure 2 show the aerodynamic surface mesh on the top skin of the swept half-wing and curved half-wing respectively.

Figure 1 Aerodynamic surface mesh of the swept half-wing model (top view) (see online version for colours)

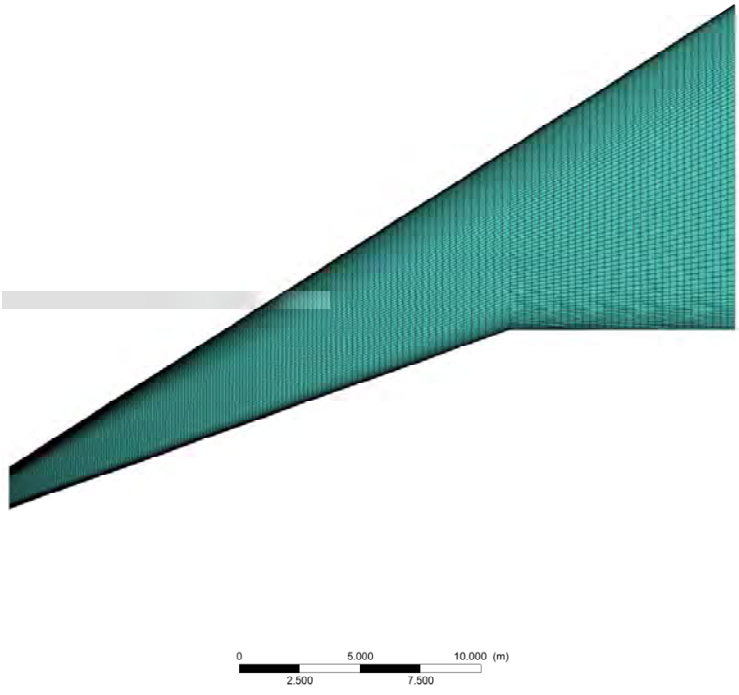

Figure 2 Aerodynamic surface mesh of the curved half-wing model (top view) (see online version for colours)

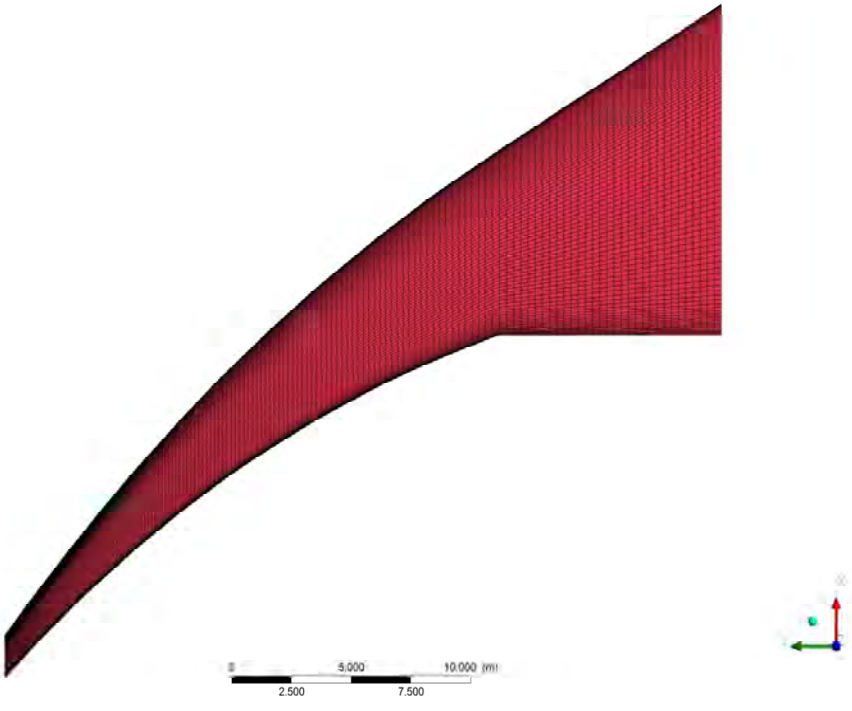

For the swept half-wing model, Figure 3 and Figure 4 show details of the aerodynamic surface mesh of the wing-tip area and the wing-root area respectively.

Figure 3 Aerodynamic surface mesh of the swept half-wing model (wing-tip area) (see online version for colours)

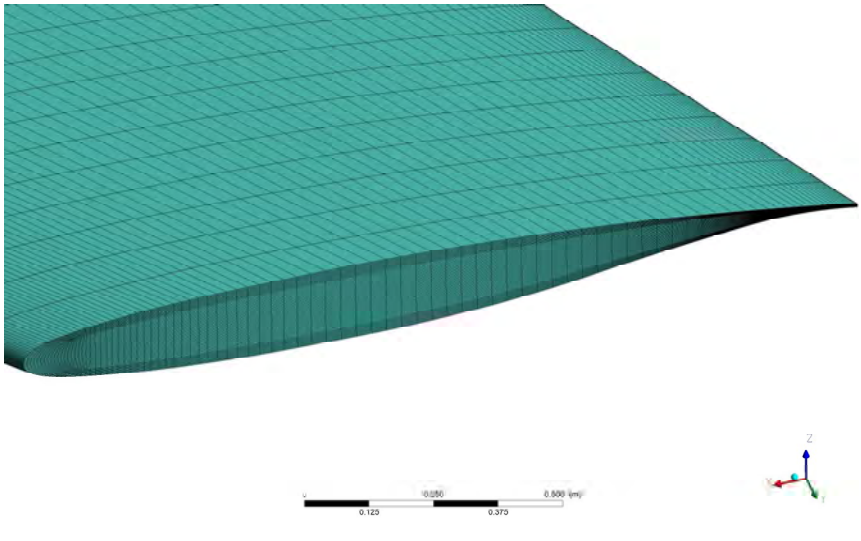

Figure 4 Aerodynamic surface mesh of the swept half-wing model (wing-root area) (see online version for colours)

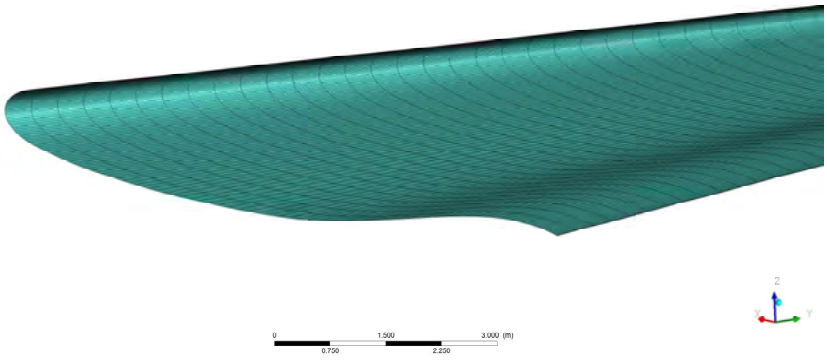

The structured meshes of the two wings were built maintaining a similar topology for both models; for this purpose, the control volumes around the wing models were built by dividing them into blocks. The dimensions of the entire aerodynamic field are: height = 131 m, width = 90 m, and length = 278 m.

Figure 5 shows, by way of example, the subdivision into blocks adopted to build the structured aerodynamic mesh for the swept wing model. A similar technique was used for the curved wing model.

Figure 5 Geometry of blocks implemented for the swept wing aerodynamic model (see online version for colours)

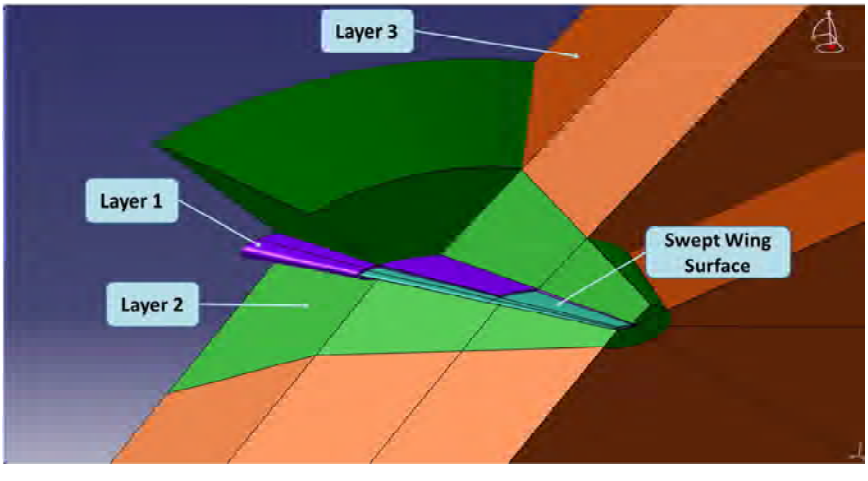

Density-based analyses were executed and the k-epsilon model was adopted as turbulence model coupled with the use of standard wall functions. In general, the present CFD results refer to high Reynolds numbers between 50×10^6 and 60×10^6 (the mean aerodynamic chord of the wing is the reference length) as indicated in Chiarelli and Bonomo (2016). For reasons related to time and computational cost, the cell sizes used near the wing surface would not have been able to simulate the viscous substrate; therefore, wall functions were used. Analysis of the aerodynamic meshes showed that the

y+ values were much greater than 30 across the entire surface for both wing models. This condition satisfied the requirement of applicability of the wall function technique to describe with sufficient approximation the airspeed profile near the wing surface. Moreover, the y+ values of the CFD meshes are adequate for the high Reynolds numbers of the present analyses. Table 2 shows the boundary conditions adopted to perform the CFD analyses.

Table 2 CFD boundary conditions on outer surfaces of the aerodynamic field

	Swept wing model	*Curved wing model*
Pressure far field	Front side up down	Front side up down
Pressure outlet	Rear	Rear
Symmetry	Centre-line plane	Centre-line plane
Wall/no slip	Wing surface	Wing surface

Figure 6 and Figure 7 show, as an example, the Mach number distribution in sectional colour maps along the wings: these maps follow the boundaries of the supersonic zone on the wings. C_L indicates the lift coefficient and M indicates the Mach number of the asymptotic flow. The results refer to rigid CFD analyses (URANS approach) of the nominal geometry of the wings under the following operating conditions: M = 0.85, C_L = 0.4, altitude = 10,000 m (the value of the lift coefficient C_L correspond to different angles of attack for the two wings).

Figure 6 Mach number: sectional colour maps for the swept half-wing model (M = 0.85, CL = 0.4, altitude = 10,000 m) (see online version for colours)

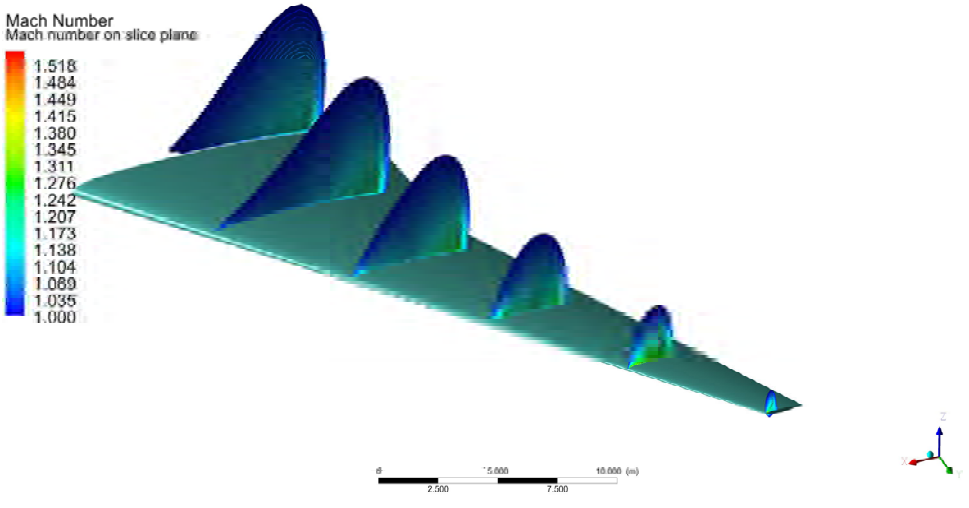

The supersonic zone on the curved wing tapers towards the wing tip: the planform of this wing softens the transonic flow characteristics.

Figure 8 shows the top view of the structural layout of the swept wing model (the spars and longitudinal stiffeners arranged on the wing skins are shown). Ribs are not visible in this image. A detailed description of the characteristics of the wing structures is available in Chiarelli and Bonomo (2016).

Figure 7 Mach number: sectional colour maps for the curved half-wing model (M = 0.85, C_L = 0.4, altitude = 10,000 m) (see online version for colours)

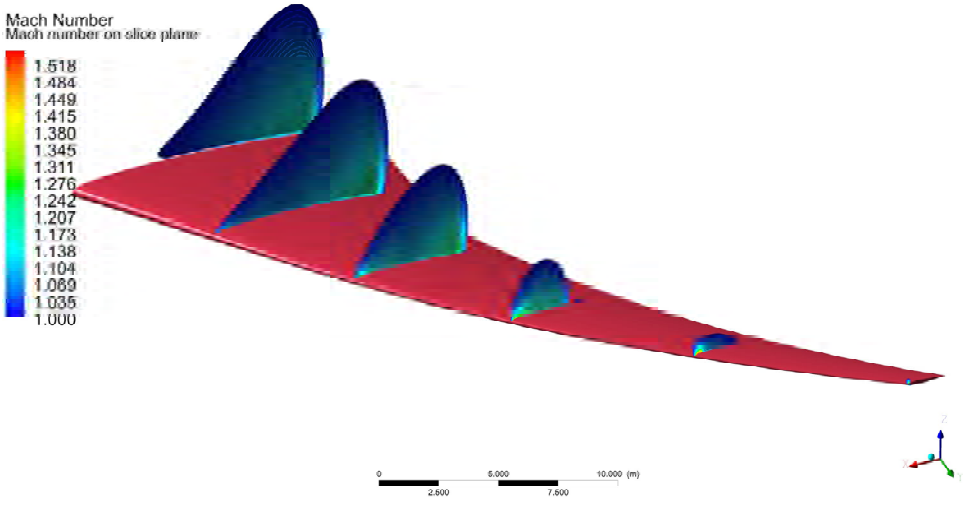

Figure 8 Structural layout of the swept wing model (geometry of the spars and stringers) (see online version for colours)

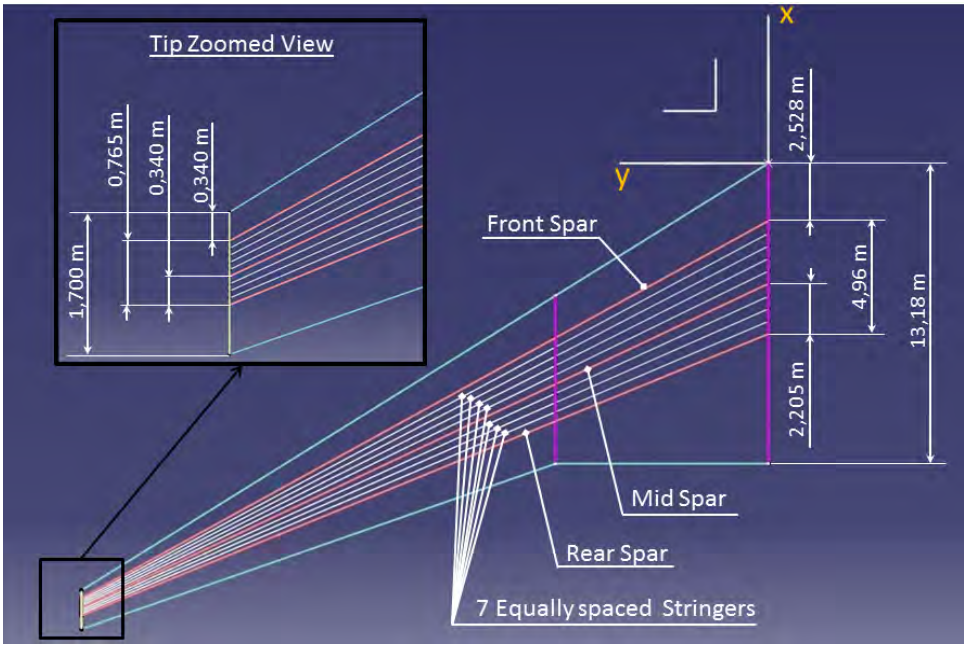

Figure 9 shows a section of the swept wing in which both the model of the internal structure and the fictitious beam elements simulating the engine nacelle and its pylon are visible. The finite element model of the wings considers the mass and moment of inertia effects of the engine installed under the wing in the kink section. For this reason, the shape of normal modes and the natural frequencies depend also on the effects of the

engine. On the other hand, to keep the complexity of the structured meshes within acceptable levels and to avoid the use of a huge number of cells during the FSI analyses, fluid dynamic models do not consider the effects that the engine nacelle and the flow produced by the engine itself have on the pressure distribution around the wings. In this regard, the post-processing of the CFD results shows that the pressure distribution on the wing regions near their kink sections is not significantly involved in the development of the instabilities. This observation justified a posteriori the use of a simplified CFD model for coupled fluid-structure dynamic analyses.

Figure 9 Internal structure for the swept wing model (see online version for colours)

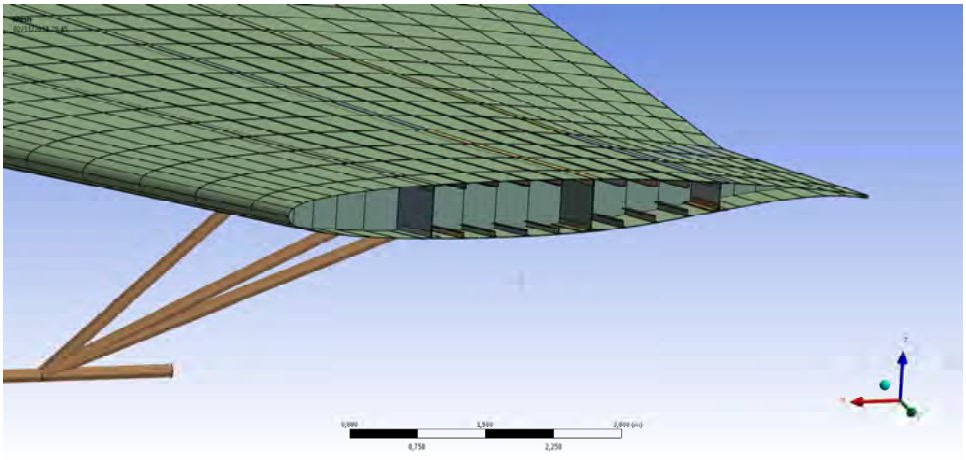

Figure 10 Graph of damping vs. mach (see online version for colours)

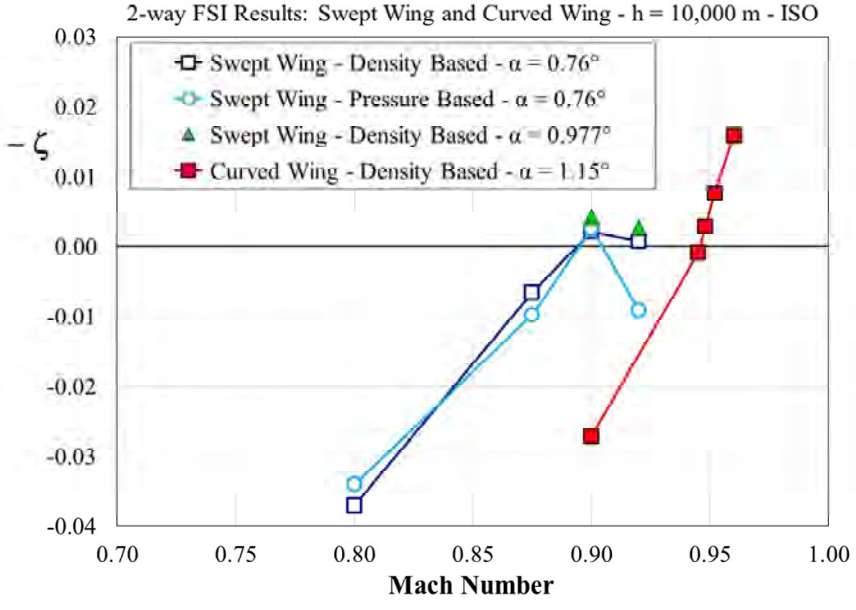

Source: Chiarelli and Bonomo (2019)

Figure 10 shows the graph of damping vs. Mach number for both wings that has been estimated from the displacement results of the 2-way FSI aeroelastic dynamic analyses presented in Chiarelli and Bonomo (2019). The plotted parameter represents the exponent of the time decay function where ς is the damping factor. It is evident from the damping diagram that the instability form of the curved wing is particularly severe compared to that of the swept wing.

In order to test the effects of different solvers, some fluid-structure analyses were performed using the pressure based solver. The density based solver is designed for high-speed compressible flows (higher accuracy in shock resolution), while the pressure based solver provides reliable results for incompressible and mildly compressible flows as shown in ANSYS Inc. (2013). In Figure 10 (h = altitude), the damping value estimated for M = 0.92 with the pressure based analysis (swept wing) is quite different from the value calculated with the density based method because the compressibility effects under such conditions become very strong. For this reason, it was decided to use the density based method for all fluid dynamic analyses.

The angles of attack of the two wings (α = 0.76º and α = 1.15º respectively) correspond to the same value of C_L = 0.4 for M = 0.85 based on the rigid CFD analyses.

As discussed in Chiarelli and Bonomo (2019), the dynamic instability of the swept wing model shows typical features of a single-degree-of-freedom-flutter. In Figure 10, near Mach = 0.90, a '*narrow region of instability*' is observable for the swept wing, and this agrees with what is stated in Dowell et al. (2003) and Dowell (2015). For Mach numbers higher than 0.90 the swept wing clearly tends to reach stable conditions. This phenomenon occurs for both numerical approaches chosen to solve the flow field equations (*density based and pressure based*). Furthermore, for the swept wing the damping depends on the angle of attack (α = 0.76º and α = 0.977º in the figure). In the transonic regime, this 'strange' variation of the overall damping as a function of Mach number (or flight speed) is typical of *flutter-buffet instability*.

On the other hand, the dynamic instability of the curved wing model consists of a *bending-torsion binary flutter* and the relationship between damping and Mach is monotonic (as is typically the case for this form of instability).

In addition, at a fixed altitude, the critical speed is higher for the curved wing compared with the swept wing (Figure 10). Previously, in Chiarelli et al. (2010), the latter result was obtained by adopting the NASTRAN® aeroelastic solver.

The different forms of instability can be qualitatively observed by analysing proper animation files of the two wing models oscillating in post-critical conditions. These files are available as supplementary material in Chiarelli and Bonomo (2019).

For both models, the '*flutter frequency*' falls in the range of first natural frequencies of the half-wing structures (Table 3 and Table 4).

Table 3 Frequencies of the first structural modes

Natural Mode Id	*Swept wing [Hz]*	*Curved wing [Hz]*
1	1.057	0.914
2	2.127	2.063
3	2.909	2.367
4	3.750	3.278
5	4.417	3.729

Table 4 Estimated flutter frequencies

Wing model	*Mode feature*	*f [Hz]*	*Mach number*
Swept	Single degree of freedom flutter (Flutter-buffet)	4.102	0.90
Curved	Two degrees of freedom flutter (Bending-torsion flutter)	3.320	0.948

Source: Chiarelli and Bonomo (2019)

Figure 11 to Figure 13 show third, fourth and fifth natural modes of vibration of the swept half-wing model, respectively. Figure 14 to Figure 16 show third, fourth and fifth natural modes of vibration of the curved half-wing model, respectively.

As will be seen, these are the structural modes involved in the forms of instability.

Figure 11 Swept wing – natural mode 3 (f = 2.909 Hz) (see online version for colours)

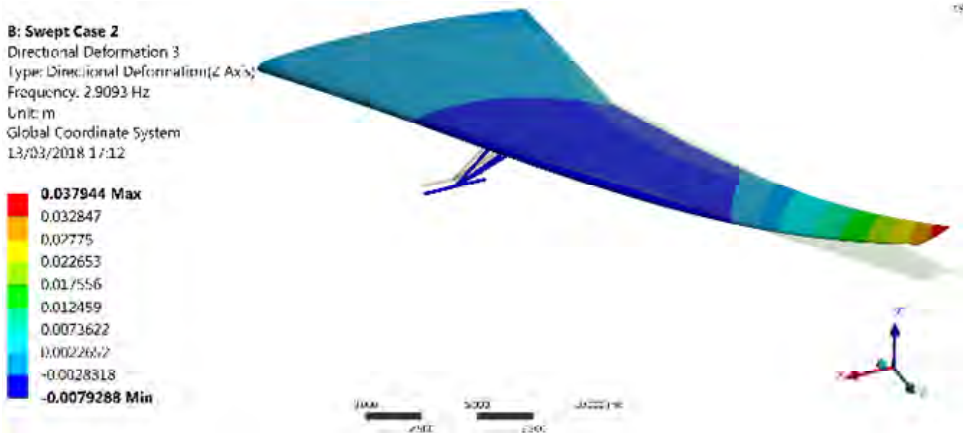

Figure 12 Swept wing – natural mode 4 (f = 3.750 Hz) (see online version for colours)

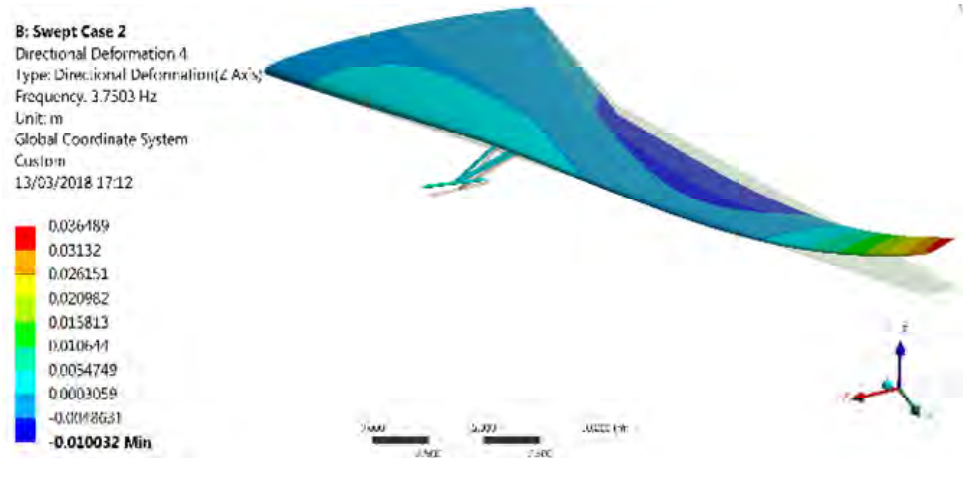

Figure 13 Swept wing – natural mode 5 (f = 4.417 Hz) (see online version for colours)

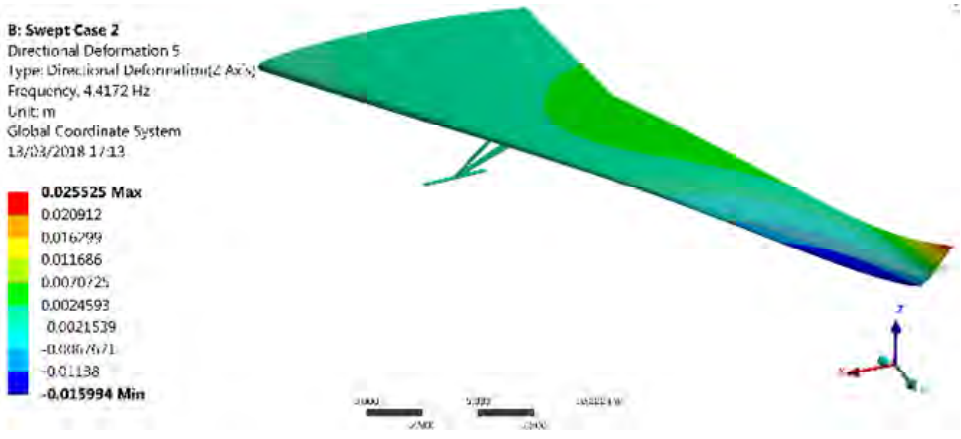

Observing the shape of the modes and their natural frequencies, we can state that the instability forms of both wings mainly involve the mechanical vibrations of the wing-tip area.

The following sections contain a more detailed discussion of the results (obtained with FSI analyses as well as with rigid CFD analyses) and a qualitative comparison between our numerical results and the literature.

This new and detailed data analysis is first based on the power spectral density (PSD) calculation for lift coefficients, drag coefficients and wing-tip displacement. In this way, the characteristic frequencies of the dynamic instability phenomena that occur for the curved and swept wing models are estimated. Secondly, we will compare these frequencies with the natural frequencies of the wings, obtained through the modal analysis, and with the frequency contents of the pressure field calculated through unsteady CFD analyses performed on rigid models. The geometry of these rigid models has been modified accordingly the displacement time histories of the wings near the instability conditions (FSI results). In this way, a preliminary, albeit indirect, investigation was executed on the interaction between structural modes and fluid modes (see also Gao and Zhang (2020)) involved in the dynamical instability of the above cases of three-dimensional transonic aeroelasticity.

As mentioned above, a sensitivity analysis was carried out in the initial phase of the research, also in order to highlight the effects of the turbulence model.

The sensitivity study, discussed in detail in Chiarelli and Bonomo (2019), involved performing several CFD analyses (performed on rigid models).This study compared the lift and drag coefficients of both wing models obtained with different levels of mesh refinement and selecting different turbulence models. In particular, the results obtained with the use of the k-epsilon model (widely used in general) and the use of standard wall functions were compared with the results of analyses performed with the realisable k-epsilon model (generally more efficient) and the adoption of the enhanced wall treatment technique. The results obtained showed that with the same mesh refinement, probably due to the high Reynolds number, the differences in the aerodynamic coefficients obtained with the two turbulence models were negligible.

Figure 14 Curved wing – natural mode 3 (f = 2.367 Hz) (see online version for colours)

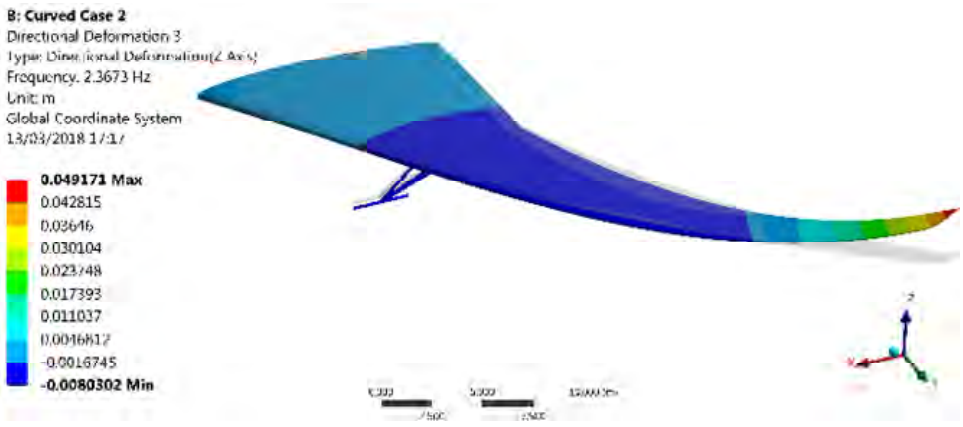

Figure 15 Curved wing – natural mode 4 (f = 3.278 Hz) (see online version for colours)

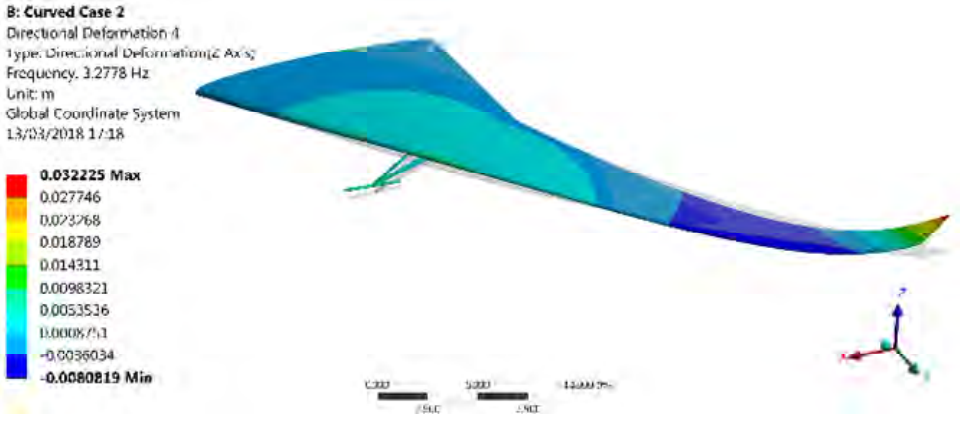

Figure 16 Curved wing – natural mode 5 (f = 3.729 Hz) (see online version for colours)

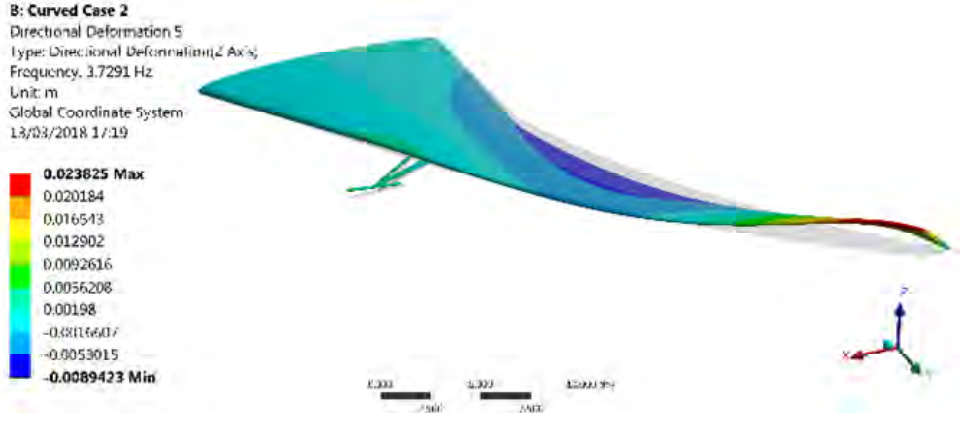

The sensitivity analysis did not involve the use of other turbulence models (such as the SST model or the k-omega model) nor a much more onerous direct numerical simulation (DNS) approach. The results obtained with the FSI analyses shows that far from the conditions of instability, large dynamic oscillations of the wings produce important oscillations of the shock waves and important phenomena of separation of the boundary layer. In these situations, probably the standard k-epsilon model is not reliable enough. However, it is also true that, near the instability conditions the dynamic oscillations are rather small (above all in the case of flutter-buffet instability): this fact partly justifies the use of a not particularly sophisticated turbulence model (no macroscopic oscillations of both the shock waves and the boundary layer are evident). Furthermore, despite having adopted the same type of aerodynamic grid and the same theoretical models, the instability shapes of the two wings appear to be very different: it can therefore be assumed that the shape of the wings predominantly dominates the instability phenomena.

2 FSI analysis: frequency content and interpretation of dynamic responses

For the fluid dynamic analyses and the fluid–structure interaction analyses, Table 5 summarises the setting parameters adopted in the ANSYS Workbench environment.

The choice of suitable step size for the FSI analysis is related to a trade-off between the time resolution required to correctly detect the phenomena in the frequency range of interest and the time cost of the analysis. A hundredth of a second satisfies both requirements adequately.

The structural damping was defined by means of Rayleigh damping model. The stiffness and mass coefficients (shown in Table 5) were defined in order to obtain a damping factor between 3% and 4% for structural modes having frequencies in the range 1 Hz ÷ 6 Hz.

Table 5 Analysis settings

ANSYS Fluent settings (transient analysis)	
Fluid	Air
Altitude [m]	10,000
Solver	Density based
Viscous model	*k-ε* standard
Standard wall function	
Time step [s]	0.01
Max iterations per time step	200
Convergence criteria	$1.0 \cdot 10^{-6}$
System coupling setting (FSI transient analysis)	
Step size [s]	0.01
Max number of coupling iterations	5
Data transfer Mechanical to Fluent	Incremental displacements
Data transfer Fluent to Mechanical	Forces
Structural damping	Rayleigh formulation
Stiffness coefficient	$1.8189 \cdot 10^{-3}$
Mass coefficient	0.43085

Figures 17 and 18 show the PSD computed for the vertical displacement of the tip leading edge from the FSI analysis of the swept wing and the curved wing, respectively. These results refer to Case 2: the second inertia distribution studied in Chiarelli and Bonomo (2019). In the figures, vertical dotted lines indicate the frequencies of the first ten natural modes of vibration of the two half-wing models. The spectral densities highlight the characteristic frequencies of the unstable aeroelastic oscillations of the wings (frequencies shown in Table 4), and the clear difference in the orders of magnitude of the two PSD graphs indicates the development of two distinct physical phenomena.

Figure 17 FSI of the swept wing: spectral density of tip leading edge displacement (see online version for colours)

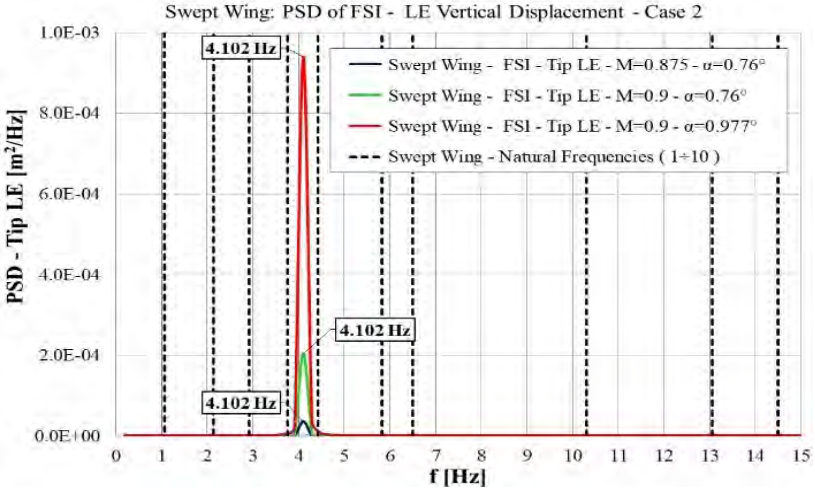

Figure 18 FSI of the curved wing: spectral density of tip leading edge displacement (see online version for colours)

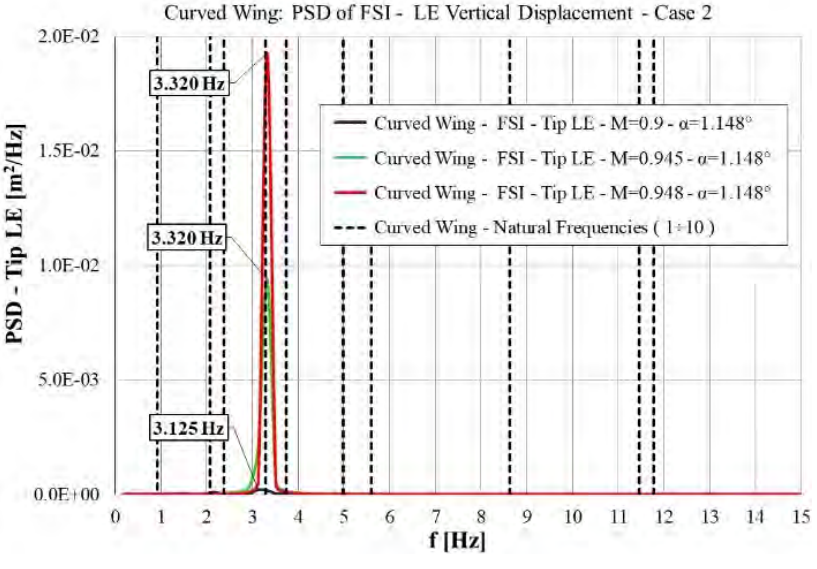

Post processing of the aerodynamic coefficients, allows us to better understand what is happening on the two wings. Figures 19 to 22 show the time histories of lift and drag coefficients C_L and C_D, from the FSI analyses, for both wings. The lift coefficients related to the swept wing model (M = 0.9, α = 0.977°) and the curved wing model (M = 0.948, α = 1.148°) are both oscillatory with an increasing amplitude. These graphs refer to unstable conditions according the overall damping data shown in Figure 10.

Figure 19 FSI of the swept wing: time history of the lift coefficient (see online version for colours)

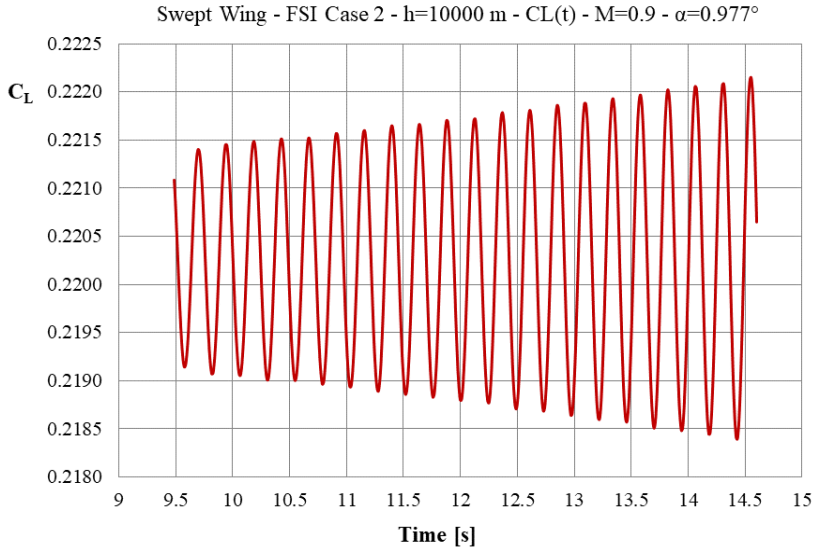

Figure 20 FSI of the swept wing: time history of the drag coefficient (see online version for colours)

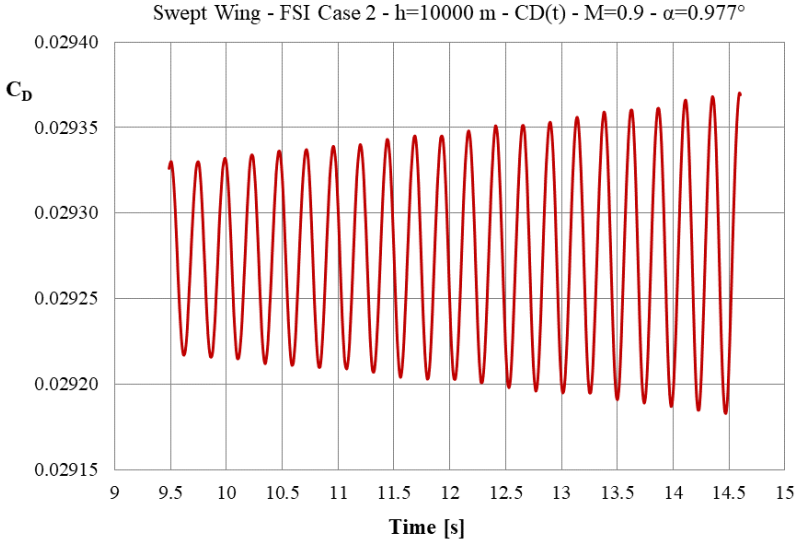

As occurs for displacements, the amplitudes of oscillations for the curved wing are greater than the amplitudes of oscillations of the swept wing.

Figure 21 FSI of the curved wing: time history of the lift coefficient (see online version for colours)

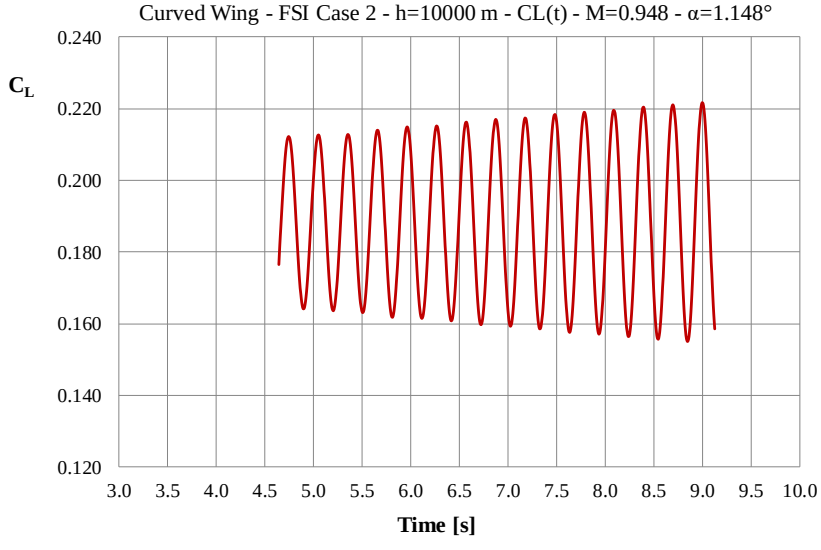

Figure 22 FSI of the curved wing: time history of the drag coefficient (see online version for colours)

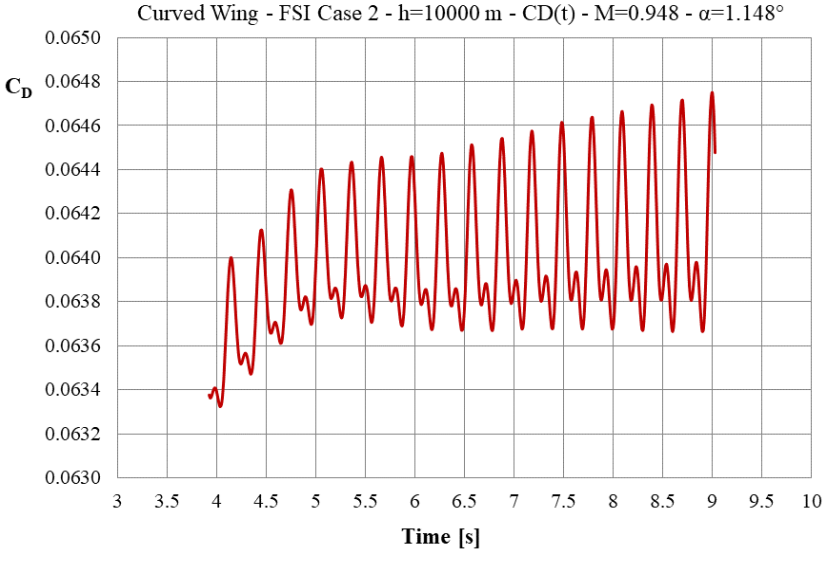

The PSDs depicted in Figures 23, 24, 25 and 26 clearly show the fundamental frequency of the resulting unstable modes, i.e., about 4.1 Hz for the swept wing and about 3.32 Hz for the curved wing (as for the PSD of the displacements). Moreover, comparing the time

histories of CD (Figures 20 and 22), for the curved wing, a second harmonic is clearly visible, due to the contribution of pitching in the aeroelastic response. On the other hand, for swept wing there appears to be no additional frequency (i.e., pure plunging occurs).

Figure 23 Swept wing model: PSD of C_L resulting from the 2-way FSI analysis (see online version for colours)

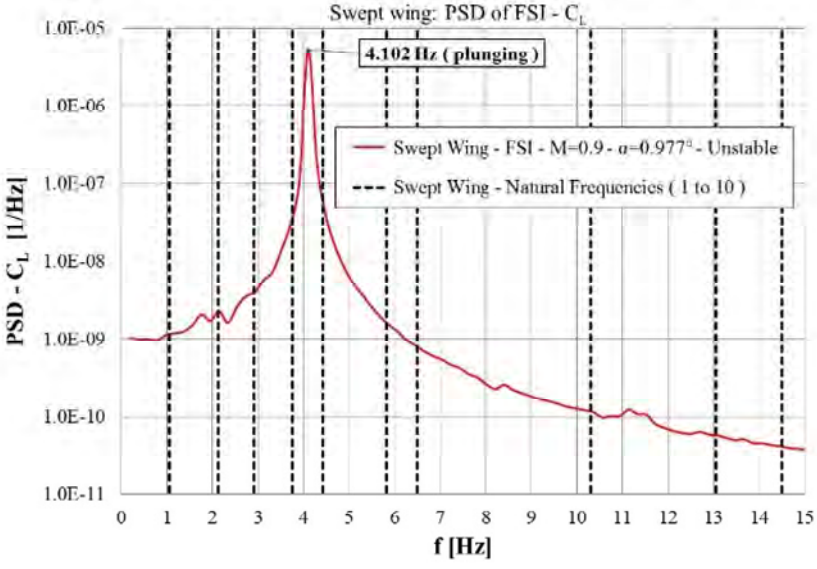

Figure 24 Swept wing model: PSD of C_D resulting from the 2-way FSI analysis (see online version for colours)

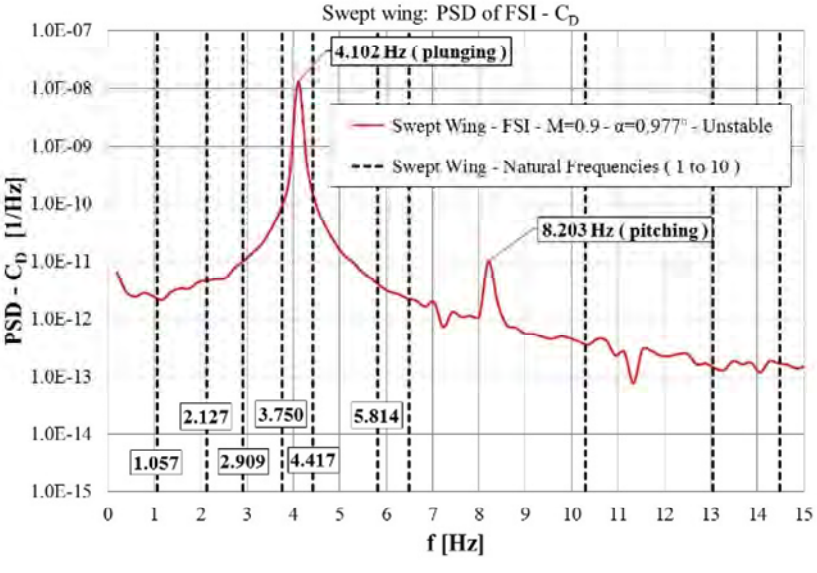

Figure 25 Curved wing model: PSD of C_L resulting from the 2-way FSI analysis (see online version for colours)

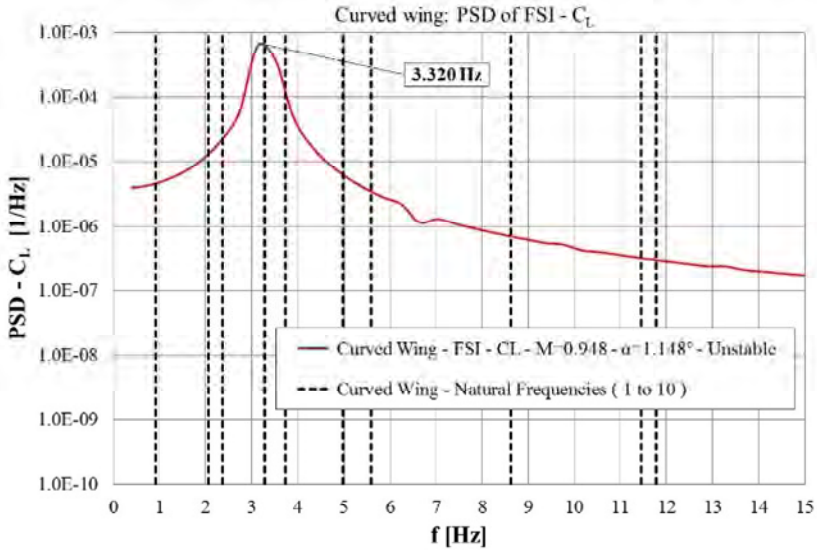

The analysis of spectral density of the two drag coefficients, as shown in Figures 24 and 26, confirms this behaviour. In fact, for the curved wing, two peaks of amplitude of approximately the same order of magnitude appear (unlike for the swept wing) and the second peak has a double frequency compared to the first (as for the swept wing).

Figure 26 Curved wing model: PSD of C_D resulting from the 2-way FSI analysis (see online version for colours)

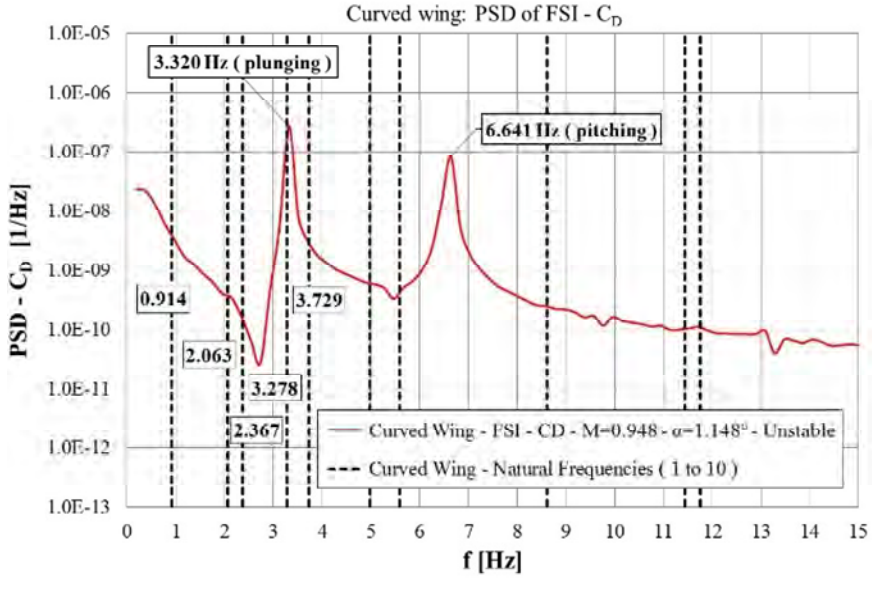

This result, expressly obtained with the FSI analyses, can be further interpreted by referring to the qualitative description of the typical oscillation motion of a wing in flutter conditions.

In a classical bending-torsion flutter, a single cycle for lift corresponds to two cycles for drag according to the following scheme:

- the sequence in pitch is *nose-up – zero – nose-down – zero – nose-up*
- the sequence in plunge is *zero – max – zero – min – zero*
- the sequence of lift coefficient is *max – zero – min – zero – max*
- the sequence of drag coefficient is *max – min – max – min – max*.

For one period of oscillation, Figures 27 to 30 qualitatively represent the sequences.

In the swept wing case, the '*pitching*' peak in the PSD graph of CD has a much smaller amplitude than the '*plunging*' peak (three orders of magnitude of difference in Figure 24). The torsional component of the motion is practically absent and then a single-degree-of-freedom-flutter occurs involving only a '*plunging*' type structural oscillation. In this case, the other '*elastic*' degree of freedom involved at the onset of the aeroelastic instability is the oscillation of the transonic pressure field interacting with the structural oscillation of the wing (a flutter-buffet interaction occurs).

As already observed, in the PSD of drag coefficient of the curved wing a second peak (f = 6.64 Hz) with the same order of magnitude (of about 10−7) of the fundamental oscillation (f = 3.32 Hz) is clearly visible in Figure 26, and then a classical bending-torsion flutter occurs involving both '*plunging*' and '*pitching*' type structural oscillations.

Figure 27 Time history of pitching (T = period of the flutter oscillation) (see online version for colours)

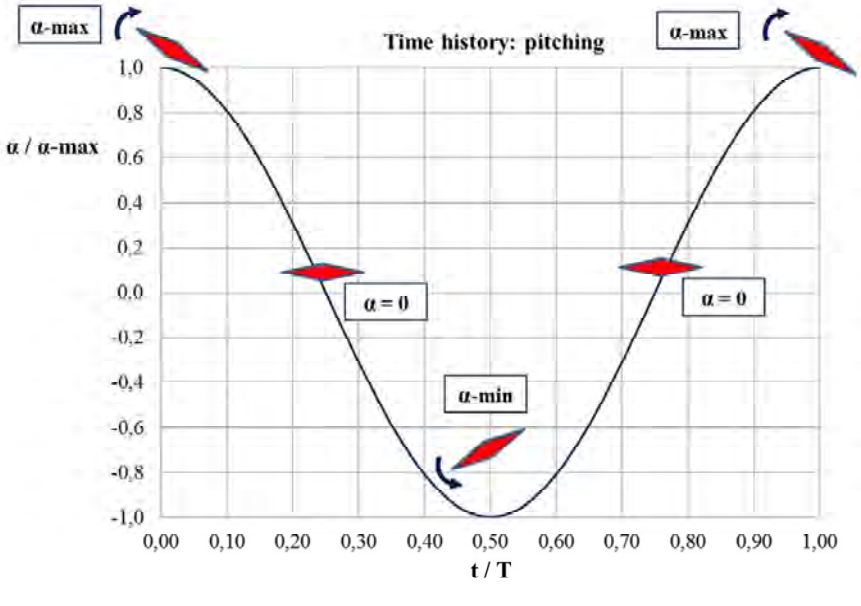

As further confirmation of what stated, it is enough to observe the intensity of the peaks of the spectral density of the lift and drag coefficients. The energy transferred from the aerodynamic field to the wing structure is much greater in the case of the curved wing, highlighting a well-defined form of instability and, at the same time, very violent in terms of flight speed (see Figure 10).

Figure 28 Time history of plunging (T = period of the flutter oscillation) (see online version for colours)

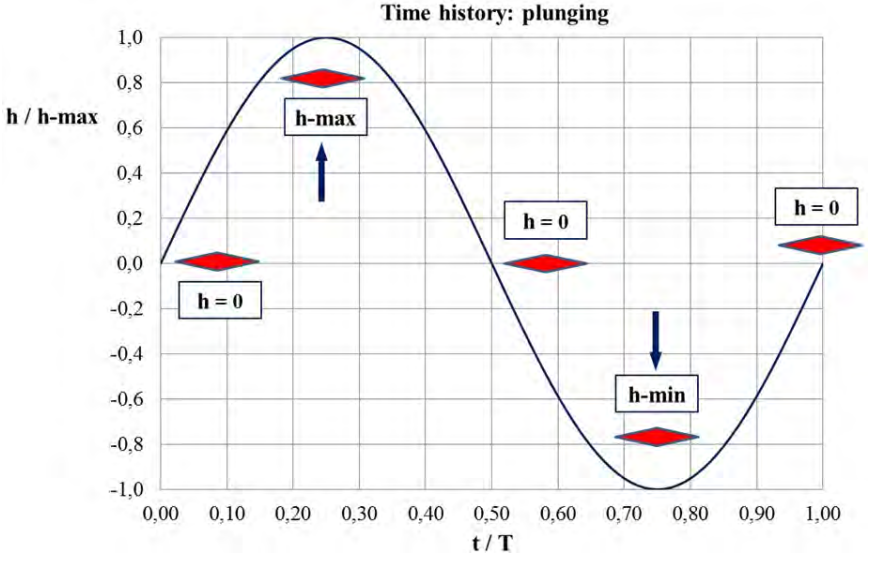

Figure 29 Time history of the lift coefficient (T = period of the flutter oscillation) (see online version for colours)

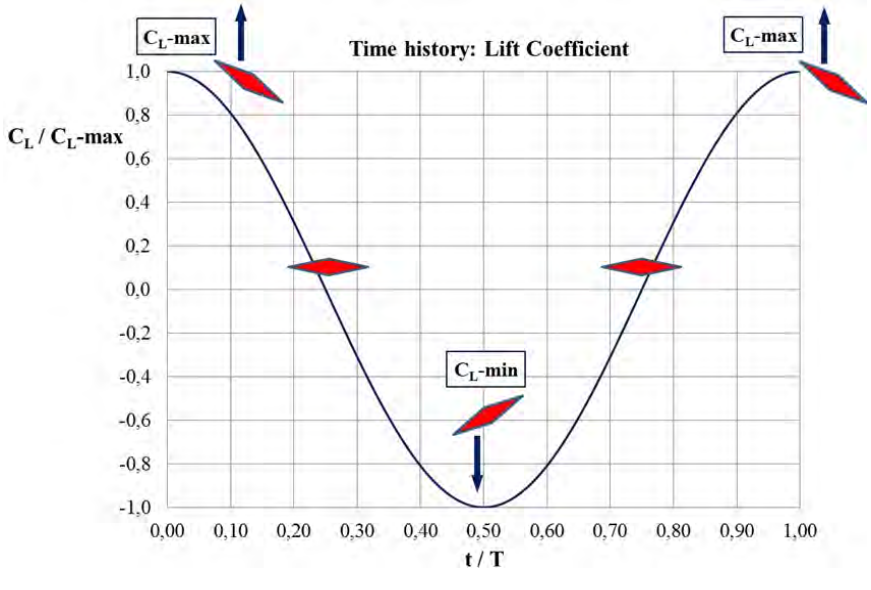

Figure 30 Time history of the drag coefficient (T = period of the flutter oscillation) (see online version for colours)

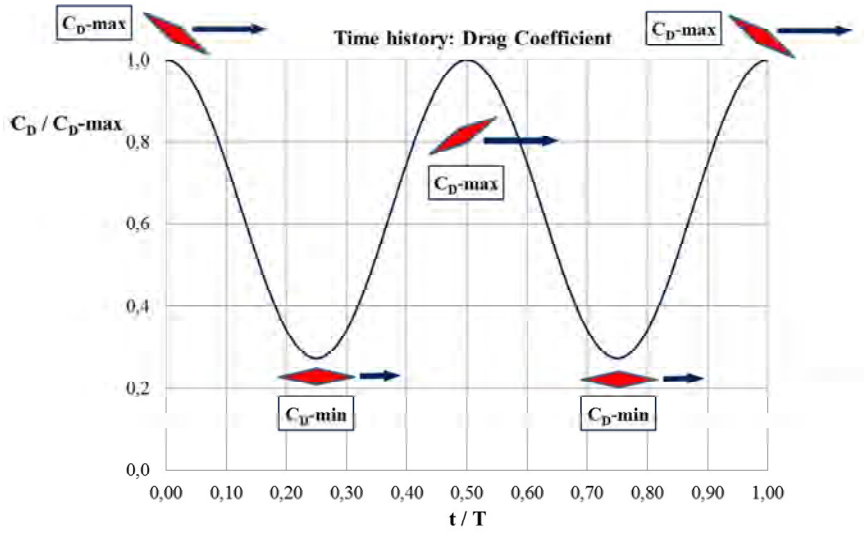

At the onset, a smaller amount of energy characterises the instability of the swept wing: in this case the work done by the aerodynamic forces does not depend on their classical combined action (in terms of frequency and phase) but on small oscillations of the pressure field around the wing surface (buffet).

The PSD graphs show that, for the curved wing, the fundamental frequency of the unstable dynamic falls between the 4th and 5th natural frequencies (natural modes of Figures 15 and 16) but its value is very close to the fourth natural frequency, which corresponds to a bending-torsion mode (Figure 15). As discussed above in the unstable regime, the curved wing response also includes a clear '*pitching*' motion (like that of mode 5 shown in Figure 16). We thus deduced that in this case, the fluid-dynamic modes do not participate directly in the instability mechanism, so that both flutter and its frequency primarily depend only on the aeroelastic interaction of first structural vibration modes (including both bending and torsion: natural modes 4 and 5).

Also for the swept wing, the fundamental frequency of the unstable mode falls between the 4th and 5th natural frequencies (natural mode of Figures 12 and 13). As discussed above, '*pitching*' does not contribute significantly to the form of instability, although in this case the 5th frequency corresponds to a *pure* torsional mode (Figure 13).

This apparent discrepancy reveals that the instability of the swept wing (flutter-buffet) involves first bending structural modes and the transonic fluid-dynamic modes, which correspond to a well-structured frequency spectrum. We will clearly identify this spectrum, for both wings, in the next section.

3 Frequency spectra of the pressure fields

To highlight the effects of the pressure field oscillations and their interaction with the elastic modes of vibration of the wings, we carried out a set of rigid transient CFD analyses in relation to specific deformed shapes of the two half wing models.

Specifically, looking at the time history responses computed during the FSI analyses, we selected the deformed shapes to be analysed under the following reference conditions:

- swept wing model: h = 10,000 m, M = 0.90, $\alpha = 0.977°$, and time t = 14.30 s
- curved-planform wing model: h = 10,000 m, M = 0.948, $\alpha = 1.148°$, and time t = 9.05 s.

These configurations correspond an average value of the dynamic displacement histories during the unstable oscillation of the wings. In both cases the Reynolds number was about 5.7×10^7.

The technique used defines a deformed shape that we could define as aeroelastic and dynamic at the same time. This deformed shape, as is well known, depends on the combined effect of inertial, elastic and above all aerodynamic actions.

It is therefore not to be confused with a simple quasi-static deformed shape resulting from 1-way analysis, because it depends on the interaction and combination of the natural modes of vibration of the wings involved in the form of instability: that is, it has the shape of the '*flutter mode*' of the wing.

Unfortunately, only a coupled and dynamic response analysis provides this deformed shape, because not only its shape but also the displacements estimate assumes great importance in the correct description of the slight fluctuations in the pressure field.

3.1 Analysis of the swept wing model results

Because we supposed there is a *flutter-buffet* for the swept wing model, to test the stability of the transonic flow, we executed a set of CFD analyses for six different values of the angle of attack imposed on the chosen deformed configuration of the wing: $\alpha = 0°$, $\alpha = 0.5°$, $\alpha = 0.75°$, $\alpha = 0.977°$, $\alpha = 1.025°$, and $\alpha = 1.1°$.

Figure 31 Swept wing: results of 'rigid' CFD on the deformed model (t = 14.30 s) (see online version for colours)

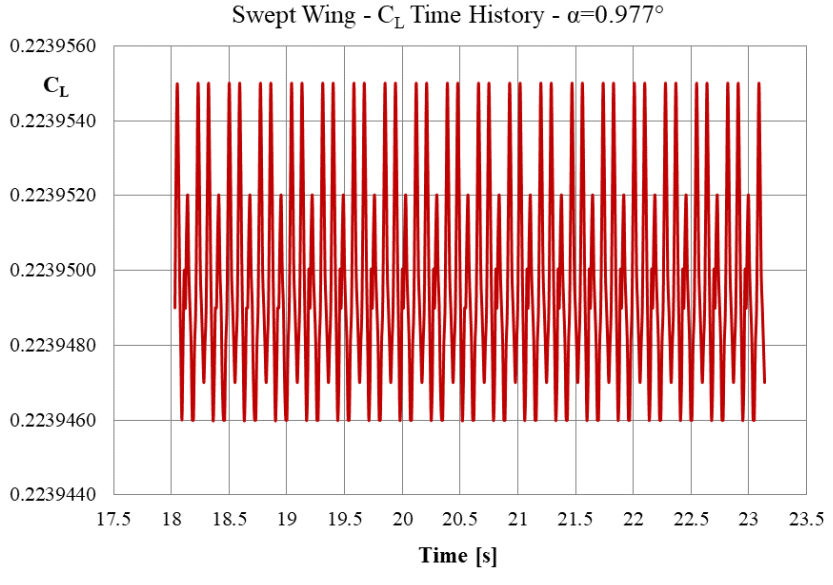

From the CFD analysis concerning the reference condition, Figure 31 and Figure 32 show parts of the CL and CD histories for to the angle of attack α = 0.977°: although the amplitude of oscillations is very small, there is a strong periodicity in the histories.

Figure 32 Swept wing: results of 'rigid' CFD on the deformed model (t = 14.30 s) (see online version for colours)

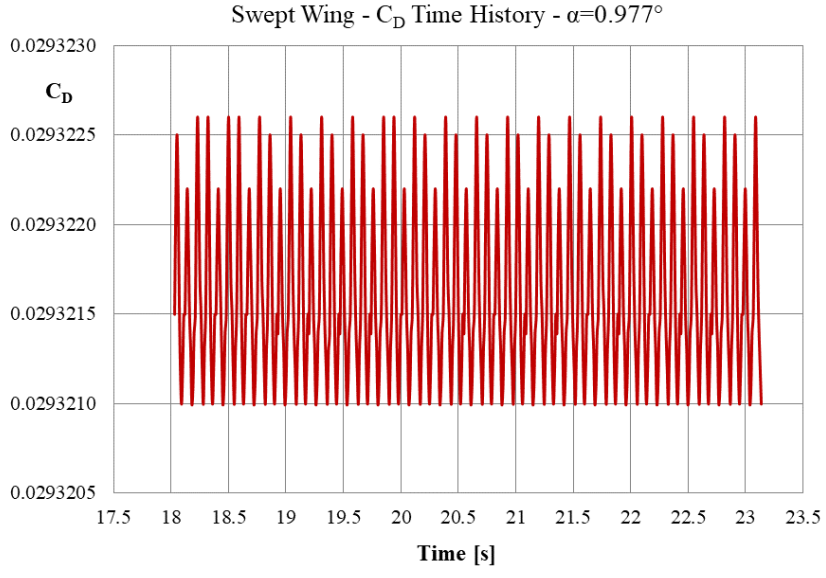

Figure 33 Swept wing: rigid CFD – spectral density of C_L (t = 14.30 s) (see online version for colours)

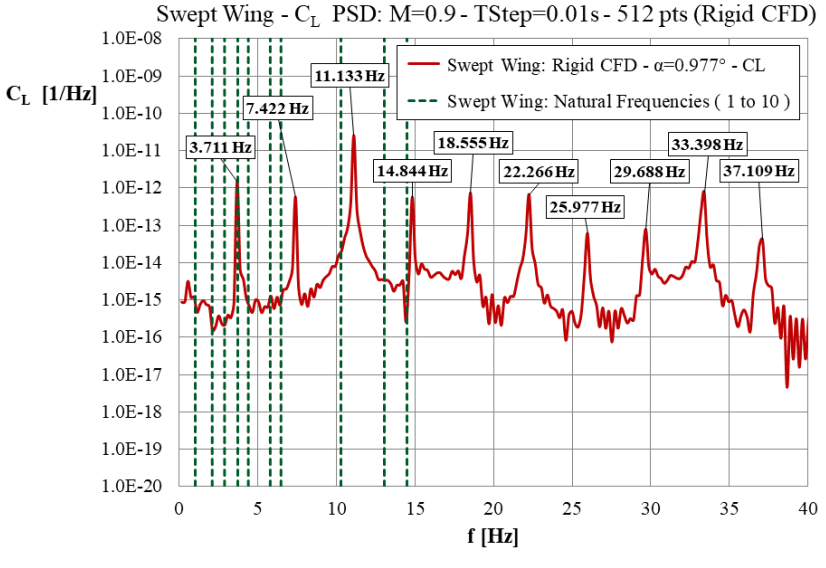

Figure 34 Swept wing: rigid CFD – spectral density of C_D (t = 14.30 s) (see online version for colours)

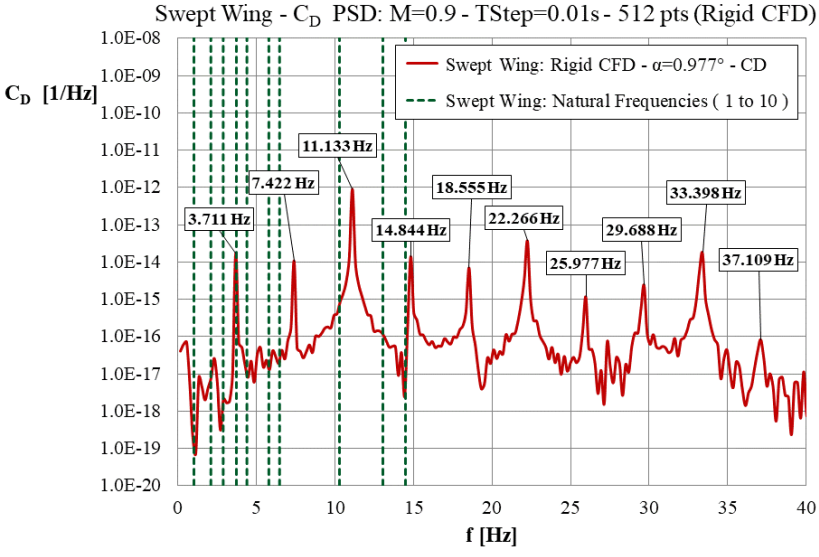

Figures 33 and 34 show the PSD of the two aerodynamic coefficients: a characteristic frequency content is evident. In the case analysed, the fundamental frequency corresponds to f1_swept = 3.711 Hz, and all the other harmonics are integer multiples of the fundamental one. Post-processing of the transient rigid CFD analysis did not reveal macroscopic oscillations of the shock wave near the wing surface, but only very small periodic changes in the shape of the supersonic bubble.

As can be observed in Figures 33 and 34, the fundamental frequency f1_swept of the pressure field falls between the first five natural modes of the swept wing, and it is very similar to the fourth natural frequency f = 3.750 Hz (see Table 3 and Figure 12).

The estimated frequency of the wing unstable response is equal to f_{FB} = 4.102 Hz (see Table 4, Figure 17 and Figure 23), but as discussed, in the transonic regime, for the swept wing, a bending type *flutter-buffet* occurs instead of a classical bending-torsion flutter. The results of the rigid CFD analysis confirm that a direct interaction between the pressure field oscillations and first structural natural modes occurred but excluding the torsional natural mode of the wing, i.e., Mode 5 (see Table 3 and Figure 13).

In fact, even if the frequency of the first pure torsional mode is $f_{Torsion}$ = 4.417 Hz (Figure 13), this mode is not directly involved in the aeroelastic instability of the swept wing, as demonstrated by a simple kinematic analysis combined with the spectral density analysis of the drag coefficient. It thus seems that higher order harmonics of pressure field oscillations participate in increasing the frequency of the swept wing unstable response up to the value of 4.102 Hz.

As previously mentioned we performed a set of analyses on the same deformed configuration of the swept wing but for different values of the angle of attack. From these analyses, we estimated the variation of the mean value of the lift coefficient (C_{Lm}) and the variation of the root means square (RMS) of C_L. Figures 35 and 36 show the aforementioned data as a function of the angle of attack. The RMSs were evaluated as the square root of the estimated area under each PSD graph of C_L (these graphs have not been

reproduced here for the sake of simplicity). As before, the lift coefficient refers to the whole model of the swept wing.

Neglecting very small nonlinear effects, the mean value of C_L (Figure 35) is a linear function with changes in the angle of attack. With a very good approximation, this fact is true near and beyond the angle corresponding to the examined *flutter-buffet* condition ($\alpha = 0.977°$).

Figure 35 Swept wing: mean value of the lift coefficient – C_{Lm} vs. α (rigid CFD) (see online version for colours)

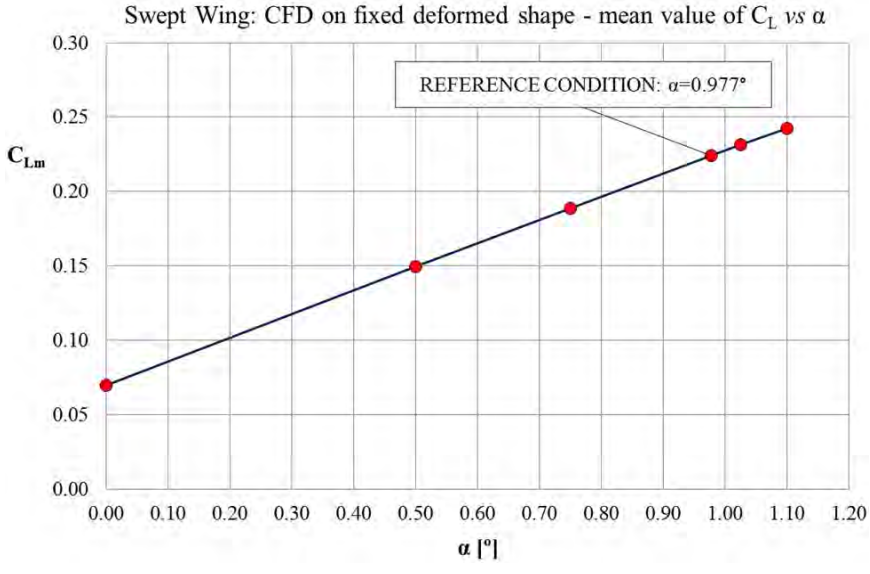

Figure 36 Swept wing – root means square of C_L vs. α (rigid CFD) (see online version for colours)

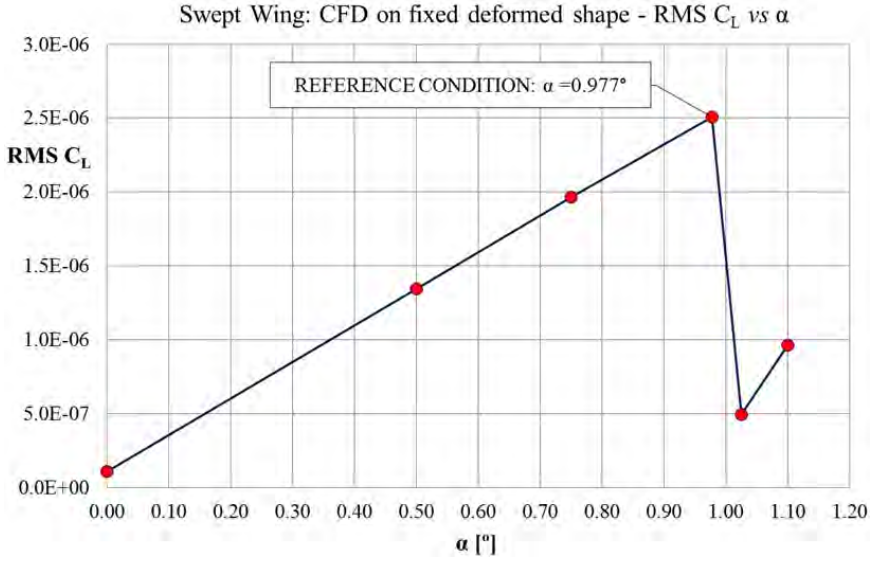

Figure 37 Swept wing: limit cycle oscillations of C_L (rigid CFD) (see online version for colours)

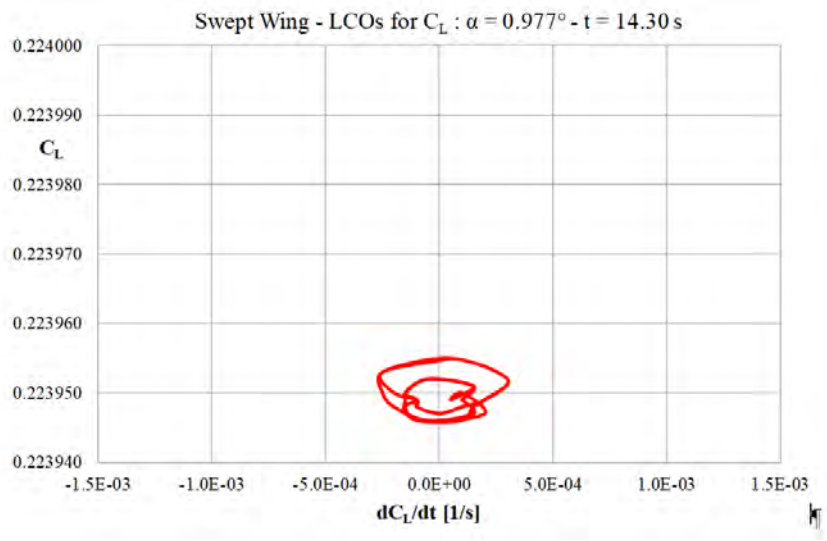

Conversely, the graph representing the RMS of C_L (Figure 36) shows an abrupt jump when the angle of attack exceeds the reference value. It is worth noting that, in *pre-buffet* conditions ($\alpha < 0.977°$), the RMS of CL is linear with respect to α.

This result highlights that, for the present configuration, there is a specific dynamic in the flow field, characterised by very small but well-structured oscillations. These oscillations also evolve towards instability conditions as the angle of attack increases. As observed, in the present case the mean value of the lift coefficient C_{Lm} is still linear for angles of attack across the aeroelastic unstable condition. This proves that, in the transonic critical conditions of the swept wing, a macroscopic flow separation downstream the shock wave is not present, and the shock wave itself does not oscillate in a macroscopic way, even though well-structured harmonic oscillations in the pressure field occur.

Figure 37 shows, from the rigid transient analysis of the swept wing, a sketch of the limit cycle oscillations (LCOs) for the lift coefficient C_L ($\alpha = 0.977°$): the plotted LCOs corresponds to the typical response of a multi-degree-of-freedom system.

Figures 38 and 39 show the distribution of the pressure RMS on the upper and lower skin of the swept wing model (h = 10,000 m, Mach = 0.90, $\alpha = 0.977°$, T = 14.30 s). In the figures, horizontal lines define four distinct zones that we used to analyse, in the post processing phase, the frequency contents of the pressure field. For both wings, the zones are defined as follows:

Zone 1 extends from the symmetry section to the wing kink (34% of half-wing span)

Zone 2 extends from wing kink to 52% of the half-wing span

Zone 3 extends from 52% to 77% of the half-wing span

Zone 4 extends from 77% of the half-wing span to wing tip.

Figure 38 Swept wing: top skin pressure RMS (rigid) in the reference condition (see online version for colours)

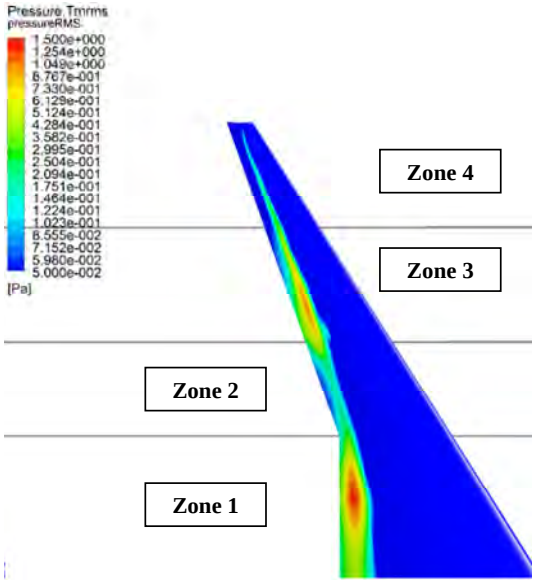

Figure 39 Swept wing: bottom skin pressure RMS (rigid) in the reference condition (see online version for colours)

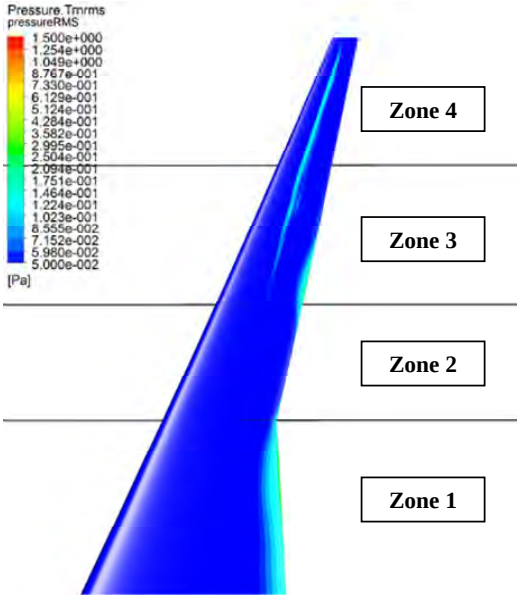

The pressure RMS is higher in the root zone (from the symmetry section to the kink section: i.e., Zone 1) and in one of the outer zones of the swept wing downstream of the shock wave (Zone 3).

3.2 Analysis of the curved wing model results

For the curved wing model a classical binary flutter instability occurs (Section 2), therefore, for this wing model, we executed a rigid CFD analysis selecting the deformed shape in a reference condition above the flutter point: Mach = 0.948, α =1.148°, t = 9.05 s.

Figure 40 Curved wing: results of 'rigid' CFD on the deformed model (t = 9.05 s) (see online version for colours)

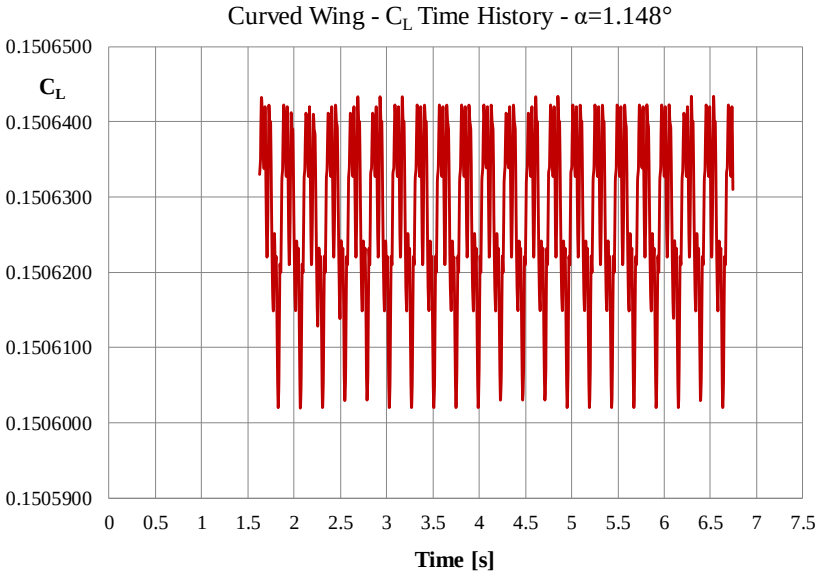

Figure 41 Curved wing: results of 'rigid' CFD on the deformed model (t = 9.05 s) (see online version for colours)

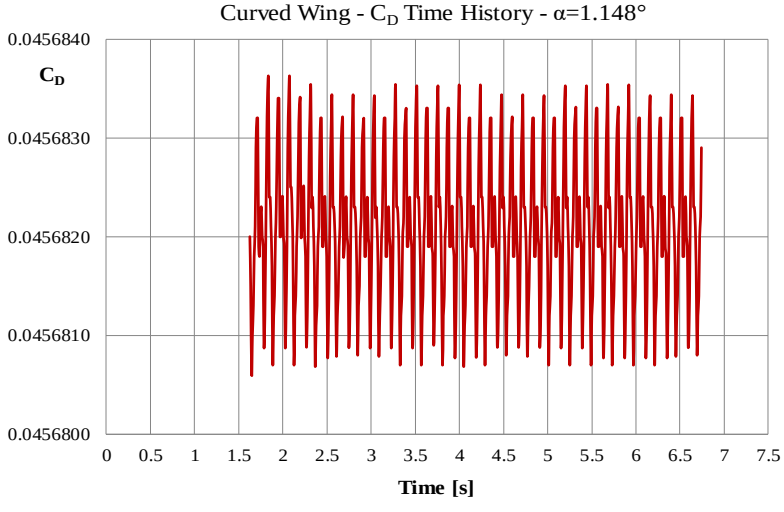

Figures 40 and 41 show parts of the histories of C_L and C_D referring to the aforementioned condition.

The amplitude of oscillations of the curved-planform wing data is higher than the swept wing data, and again there is a clear periodicity of the time histories.

Figure 42 Curved wing: rigid CFD – spectral density of C_L (t = 9.05 s) (see online version for colours)

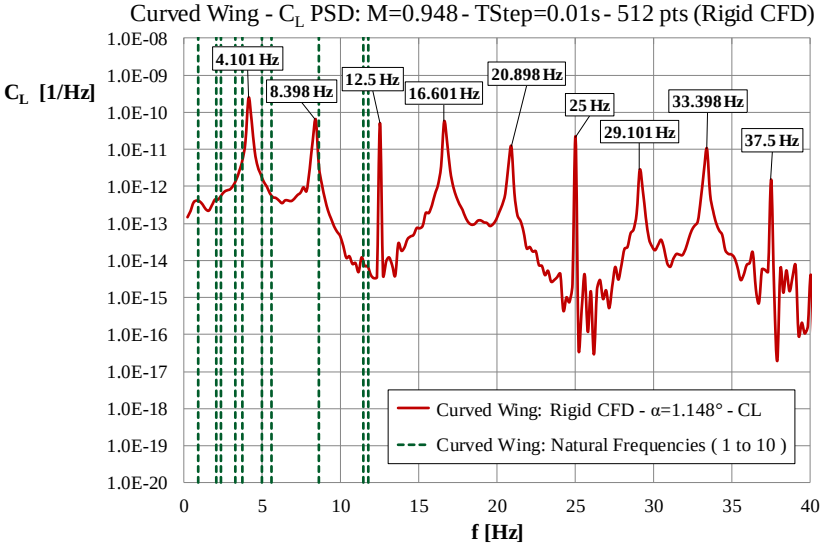

Figure 43 Curved wing: rigid CFD – spectral density of C_D (t = 9.05 s) (see online version for colours)

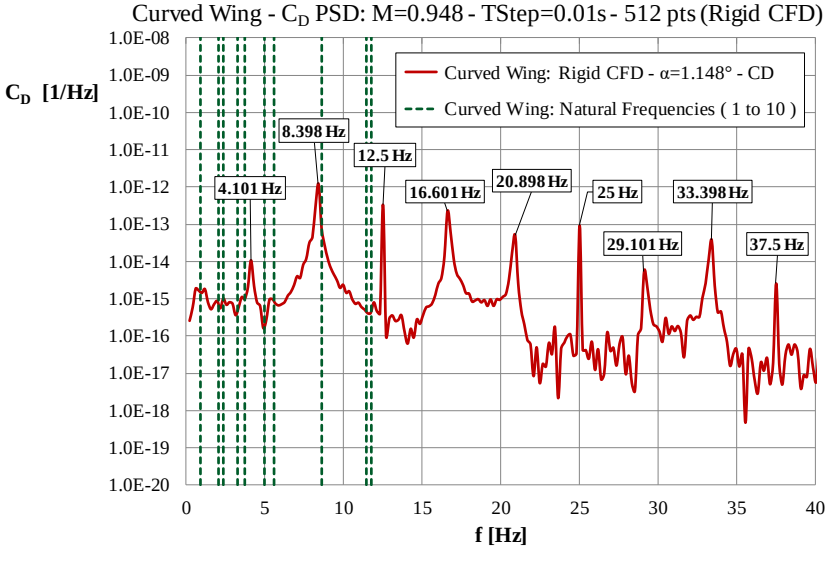

Figures 42 and 43 show the Spectral Density calculated from the time histories of the two aerodynamic coefficients. As in the previous case, a characteristic frequency content stands out. The fundamental frequency corresponds to f1_curved = 4.101 Hz, and all the other harmonics are integer multiples of the fundamental one.

Figure 44 shows the graph of LCOs of the lift coefficient: as in the case of the swept wing, the feature of these LCOs corresponds to a multi-degree-of-freedom system.

A comparison of Figure 37 with Figure 44 (graphs with the same scale) shows that, in the curved-planform wing case, the energy involved in the pressure field oscillations is higher (the Mach number is higher and the angle of attack is higher). Moreover, the fundamental frequency of these oscillations (f1_curved = 4.101 Hz) is higher than the natural structural frequencies involved in the flutter instability (Figures 18, 25, and 26 clearly show that the flutter frequency of the curved-planform wing is f_F = 3.320 Hz between 3.278 Hz and 3.729 Hz, i.e., between the 4th and 5th natural vibration frequencies). This fact proves that in the aeroelastic instability of the curved-planform wing, the transonic fluid dynamic modes do not participate directly and a classical bending-torsion flutter develops.

Figure 44 Curved wing: limit cycle oscillations of C_L (rigid CFD) (see online version for colours)

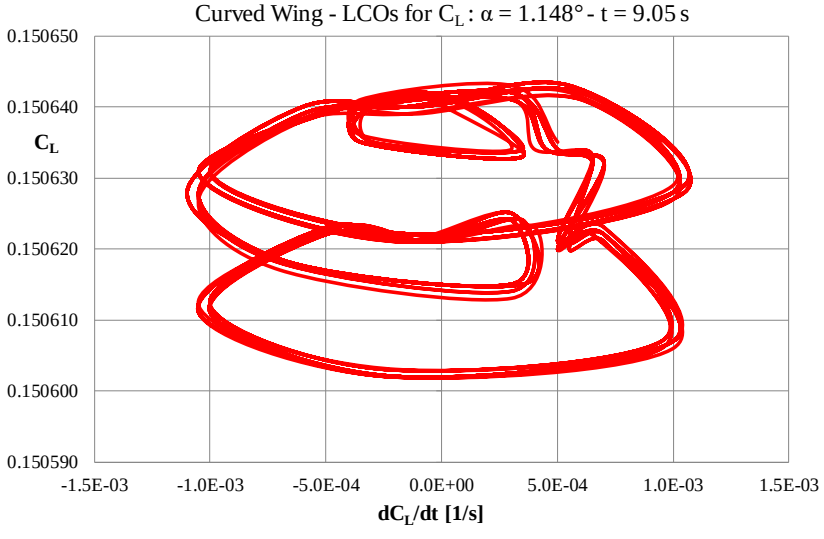

Figures 45 and 46 show the distribution of the pressure RMS on the upper and lower skins of the curved wing model (h = 10,000 m, Mach = 0.948, α = 1.148°, t = 9.05 s).

The RMS pressure contour plots have the same scale and therefore a direct comparison can be made between the swept wing (M = 0.90, Figures 38 and 39) with the curved wing results (M = 0.948, Figure 45 and 46). On the curved wing most of the energy content of the pressure oscillations is concentrated between the symmetry section and the kink section (Zone 1 in Figures 45 and 46) where the wing structural model is very stiff. On the other hand, on the swept wing the energy content develops considerably also along the wingspan (Zone 3) and not only in the root zone (Zone 1) therefore, in this case, the pressure oscillations can cause bending displacements, albeit small.

Figure 45 Curved wing: top pressure RMS (rigid) in the reference condition (see online version for colours)

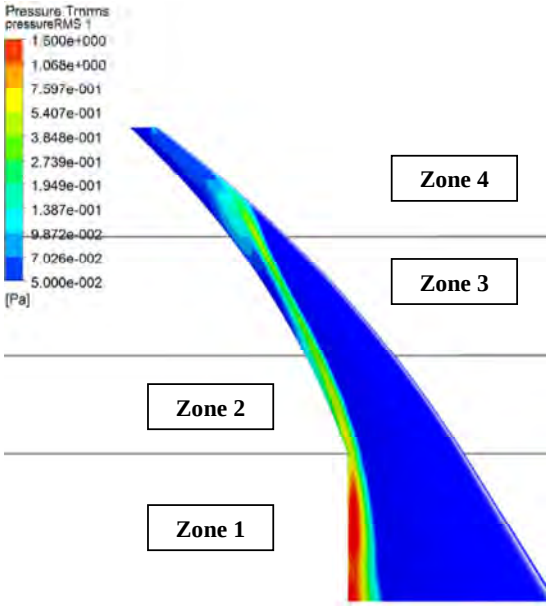

Figure 46 Curved wing: bottom pressure RMS (rigid) in the reference condition (see online version for colours)

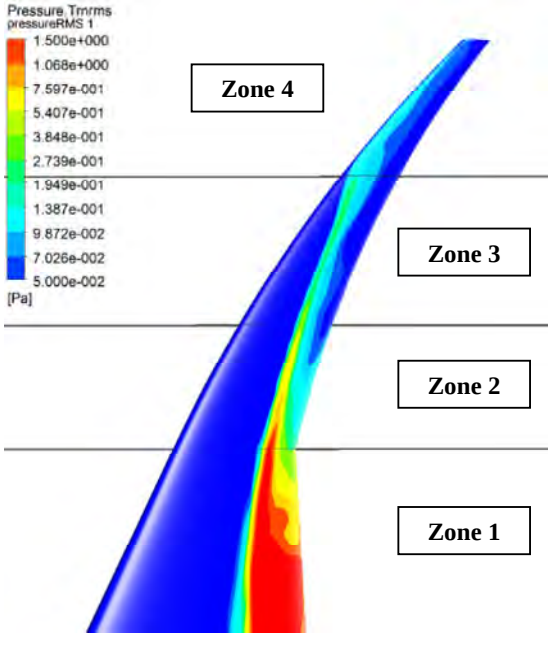

3.3 Comparison of the rigid CFD results: planform effect on pressure fluctuations

Starting from the results of the rigid fluid dynamic analyses, we performed a detailed post processing by computing the spectral density of physical parameters along four distinct zones of each wing model.

In general, it should be noted that the observed different energetic levels depend on the different Mach number values used for the unsteady CFD analyses of the two wing models performed at similar flight altitudes. That said, as an example, in this article, we compare the spectral density of the lift coefficient calculated for each separate zone of the two wings.

Figures 47 and 48 show the graphs of the PSD of C_L for each zone of curved wing and swept wing, respectively. For the curved wing, pressure fluctuations occur mainly in the root zone (yellow curve – Zone 1); while in the case of the swept wing, the pressure oscillations are very important also along the span (red curve – Zone 3).

Figures 49 and 50 show the graphs of the RMS of C_L evaluated, zone by zone, as the square root of the area under the PSD graphs of the curved wing and the swept wing respectively (the scales in the graphs are similar). For the curved wing (Figure 49), the RMS of C_L decreases monotonically along the span direction, whereas in Zone 3, the swept wing data show a relative maximum (Figure 50), and its value is twice that of the corresponding value of Zone 3 of the curved wing model. This latter result confirms that, at about 2/3 of the span, for the examined conventional swept geometry, the energy content of the pressure oscillations is higher than the examined curved wing configuration, although the Mach number in the swept wing case is significantly lower.

The different energy distributions of the two flow fields, highlighted and quantified by the present analyses, depends only on the different planforms of the wings, thus the planform strongly drives the dynamics of the pressure field in transonic regime.

Figure 47 Curved wing: PSD of C_L on zones (see online version for colours)

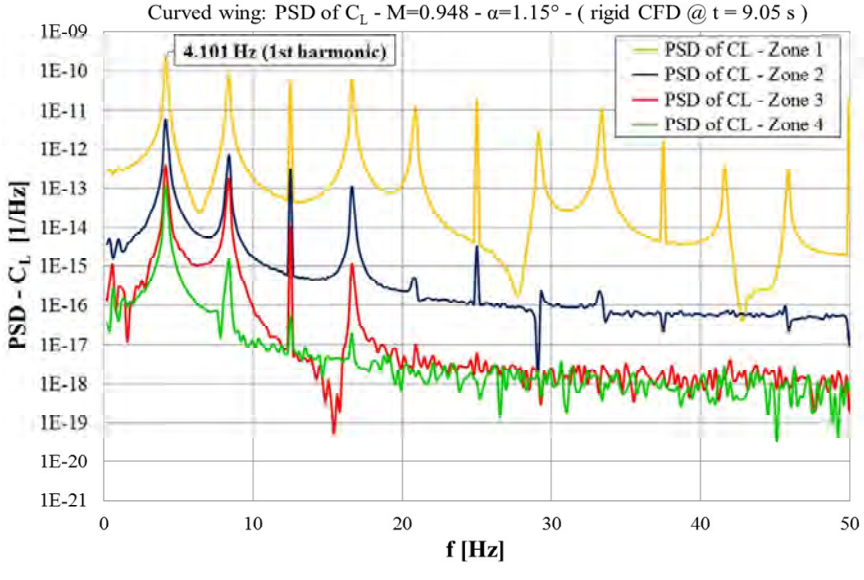

Figure 48 Swept wing: PSD of C_L on zones (see online version for colours)

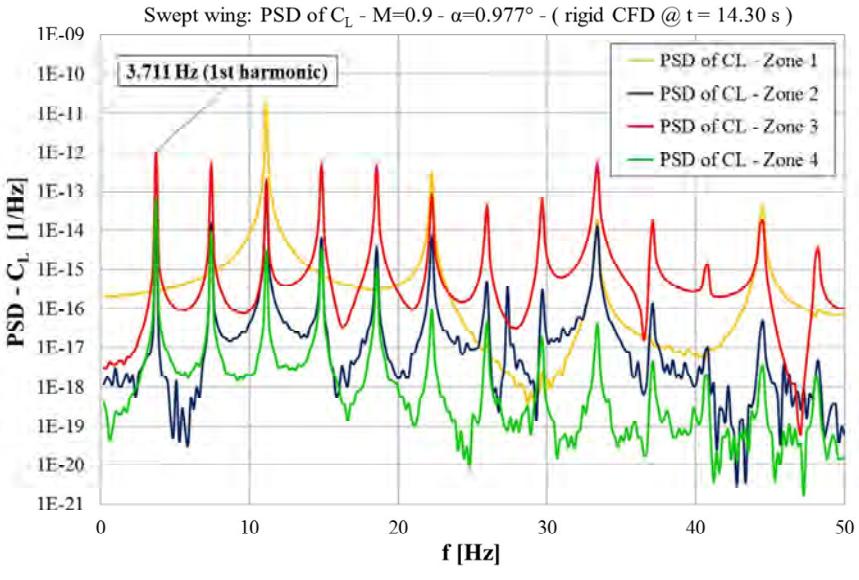

Figure 49 Curved wing: rigid CFD – RMS of C_L (see online version for colours)

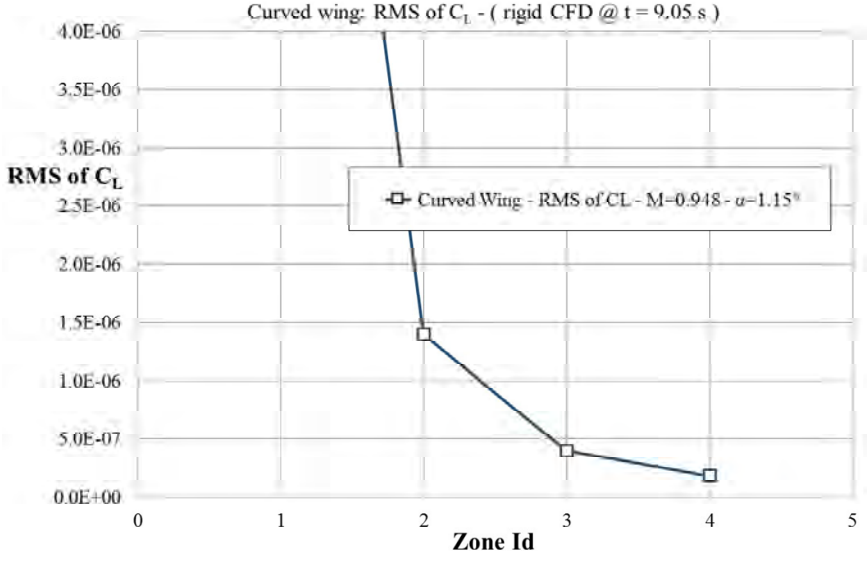

Table 6 summarises the first harmonics of the transonic fluid dynamic fields for the two wing models analysed in the present research. As discussed above, our unsteady CFD analyses were performed on rigid pre-deformed models.

Figure 50 Swept wing: rigid CFD – RMS of C_L (see online version for colours)

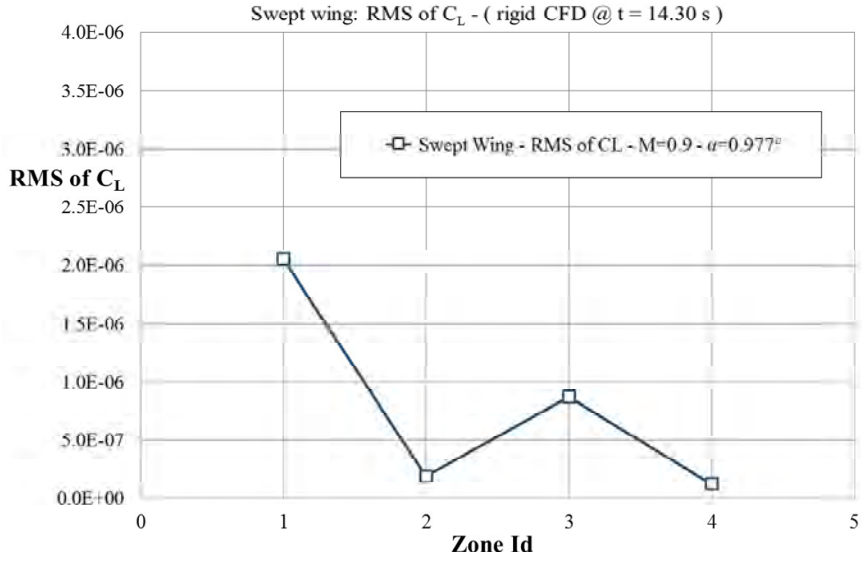

In Timme (2019), for a three-dimensional pre-deformed swept wing configuration (the NASA common research model (CRM), Vassberg et al. (2008), computation of the spatial structure of the unstable eigenmode (related to a shock buffet instability) shows that the critical zone corresponds to about two thirds of the wing span. This result agrees with our results. To this end, see Figure 4 and Figure 5 in Timme (2019); specifically, compare the Figure 5, which shows *both eigenvalue spectra at three different angles of attack approaching (and beyond) shock-buffet onset and the corresponding spatial structure of representative modes at* α = 3.75° and Mach = 0.85, with our results shown in Figures 38 and 50.

Table 6 Estimated frequencies of first fluid modes (present research)

Mode Id	*Swept wing [Hz]*	*Curved wing [Hz]*
1 – Fundamental	3.711	4.101
2	7.422	8.398
3	11.133	12.500
4	14.844	16.601
5	18.555	20.898
6	22.266	25.000
7	25.977	29.101
8	29.688	33.398
9	33.398	37.500
10	37.109	–

The CRM was originally conceived as an aerodynamic benchmark and as such, the wing geometry corresponds to the deflected shape at the nominal 1-g flight condition. In addition, during the tests the wind tunnel model undergoes further aeroelastic

deformations, which depend on aerodynamic loads acting on the model (Figure 2 of Tinoco et al. (2018)). However, these additional deformations do not correlate to the assumed real flight conditions in Tinoco et al. (2018) only the twist distributions are provided but not the bending deflections). Lastly, in Timme (2019) the critical mode evolves to the shock-buffet due to a *variation in the angle of attack of only a few hundredths of a degree*.

The analysis of the technical literature together with our results highlight that the structural deformations strongly influence the transonic buffet onset for high aspect ratio flexible swept wings and therefore, in this field, the correct estimation of the shape of the aerodynamic surfaces is fundamental in both numerical and experimental activities.

4 Conclusions

In this work, using unsteady CFD analyses together with a series of fluid-structure interaction analyses, the transonic aeroelastic instabilities of two high aspect ratio wing models were characterised.

The numerical study of the wings, a conventional swept wing and a curved-planform wing, highlights how the oscillations of the pressure field can influence the onset of transonic instabilities.

The ANSYS Workbench commercial software was adopted to perform all the analyses. The numerical models were implemented at the University of Pisa during a study carried out on a comparative investigation of the aeroelastic performance of a curved-planform wing. Such a wing provides a notable reduction in the wave drag effects and an enlargement of the high-speed aeroelastic stability margin.

Performing rigid CFD transient analyses on appropriate deformed geometries of the wing models (the deformed shapes correspond to the average displacements occurring during the unstable aeroelastic oscillations of the wings) was observed that, near unstable conditions, the pressure fields around the wings harmonically oscillate according to the dynamics of a multi-degree-of-freedom system (as occurs in a pressure waves propagation phenomenon). A fundamental frequency clearly characterises the pressure field spectra, and all other harmonics are integer multiples of the first one.

In the rigid transient analyses, the Mach numbers and the angles of attack correspond to unstable or marginally stable conditions identified with the FSI analyses of both wings. In the examined transonic conditions, the amplitudes of the pressure field oscillations are very small (macroscopic oscillations of the shock waves with large-scale separation of the boundary layer do not occur), so the assumption of small perturbations is certainly satisfied.

The frequency spectra of the fluid dynamic fields were identified by calculating the power spectral density of the aerodynamic coefficients of the wings.

Although, for both wing models, the fundamental frequency of the spectrum falls within the range of first structural natural frequencies, only for the swept wing can be observed a remarkable interaction between the structural and fluid-dynamic vibrations. This interaction provided a form of dynamic instability (flutter-buffet) involving a bending structural mode (a plunging mode) and all the first fluid dynamic modes (despite the very low energy level of the dynamic oscillations of the transonic pressure field). On the other hand, for the curved wing model the well-structured dynamics of the transonic pressure field did not interact with the elastic deflections, and a classical form of binary

flutter (bending-torsion flutter) occurred with a frequency intermediate to those of the structural modes involved.

The results discussed in this paper, based on the post processing of both 2-way dynamic fluid-structure interaction analyses and rigid transient fluid-dynamic analyses, prove that the planform plays a very important role in the transonic instability of high aspect ratio wings.

Furthermore, the same results show that, in the transonic regime, the physics of the pressure fields can determine the onset of dynamic instabilities in 'a very underhand' way. To best highlight the properties of the pressure field, in the transonic regime, authors suggest that both the numerical analyses and the experimental activities should be carried out considering the average aeroelastic-dynamic shape of a wing near the instability conditions and not a simple quasi-static shape such as the classic 1-g configuration. Any very small change in the shape of aerodynamic surfaces has a strong influence on the onset of aeroelastic instabilities.

The shape of the deflected wing to use is that of the specific 'flutter mode' (unstable mode of the wing). On the other hand, only through an analysis of the dynamic response, it is possible to recover the exact entity of the displacements to be assigned to the deformed model of the wing.

Turbulence models certainly influence the dynamic response of aerodynamic surfaces in unstable conditions, i.e., for Mach numbers much higher than the value corresponding to flutter or flutter-buffet. Based on the results of this study, albeit preliminary from this point of view, for small oscillations, i.e., around the conditions of instability, the use of different turbulence models produces not particularly different results.

On the other hand, it is known that the stiffness of the wing structure, as well as the distribution of the masses, strongly influence the dynamic response of a wing, especially for high aspect ratios. In general, one of the design techniques used to delay the onset of a bending-torsion flutter mechanism consists in suitably spacing the first natural frequencies of the wing by raising the torsional frequencies as much as possible. Torsional frequencies increase as torsional stiffness increases: it depends on the size and configuration of the sections of the wing box.

For conventional wing configurations (swept wings), in the case of flutter-buffet instability, a suitable design strategy, necessarily iterative and certainly very expensive from a computational point of view, should consider the effects of the aeroelastic response of the wing under the action of multi-frequency pressure field, which in turn depend on the dynamic response of the wing itself. In this case, however, the technical reference is the fundamental frequency of the pressure field. A design requirement could therefore consist in modifying the first frequencies and the first natural modes of the wing in order to avoid their coupling with the forcing spectrum frequencies.

A possible development of the research activity will concern the implementation of the coupled fluid-structure calculation considering the wings connected to the fuselage of an aircraft (thus adding the effects of the degrees of freedom of rigid motion) and the study of possible antisymmetric instability conditions. Simulation of the effective geometry of the engine nacelles and their effect on the aerodynamic field could be a further activity to be integrated.

Possible experimental activities, of a much different scope, could concern the accurate measurement of the frequency content of the pressure field around wing models to be tested in a transonic wind tunnel using, for example, techniques similar to those of Feldhusen-Hoffmann et al. (2018). The geometry of the models could be generated based

on the results of purely numerical aeroelastic analyses in order to verify the effect of the deflections of unstable mode on the pressure field oscillations. In the first instance, numerical models and experimental models should have the same scale.

The results of this study show that the effects of the pressure field oscillations are evident, at least from a numerical point of view, in the transonic regime. The planform of the wing is one of the design features that would seem to be very important in removing the causes of the buffet onset.

Experimental studies of a comparative type, between a conventional swept wing and a curved planform wing, could justify the use of this last design solution for future aircraft configurations.

References

ANSYS Inc. (2013) *ANSYS-FLUENT User's Manual, Rel.* Vol. 15.

Chiarelli, M.R. and Bonomo, S. (2016) 'Aeroelastic analysis of wings in the transonic regime: planform's influence on the dynamic instability', *International Journal of Aerospace Engineering*, Vol. 2016, Article ID 3563684, p.13.

Chiarelli, M.R. and Bonomo, S. (2019) 'Numerical investigation into flutter and flutter-buffet phenomena for a swept wing and a curved planform wing', *International Journal of Aerospace Engineering*, Vol. 2019, Article ID 8210235, p.19.

Chiarelli, M.R., Cagnoni, M., Ciabattari, M., De Biasio, M. and Massai A. (2010) 'High aspect ratio wing with curved planform: CFD and FE analyses', *Proceedings of the 27th Congress of the International Council of the Aeronautical Sciences (ICAS '10)*, Nice, France, pp.1524–1533.

Dowell, E., Edwards, J. and Strganac, T. (2003) 'Nonlinear aeroelasticity', *Journal of Aircraft*, Vol. 40, No. 5, pp.857–874.

Dowell, E.H. (2015) *A Modern Course in Aeroelasticity*, Springer, Cham, Switzerland.

Feldhusen-Hoffmann, A., Statnikov, V., Klaas, M. and Schröder, W. (2018) 'Investigation of shock–acoustic-wave interaction in transonic flow', *Experiments in Fluids*, Vol. 59, No. 15, https://doi.org/10.1007/s00348-017-2466-z.

Gao, C. and Zhang, W. (2020) 'Transonic aeroelasticity: a new perspective from the fluid mode', *Progress in Aerospace Sciences*, Vol. 113, Article ID 100596.

Gao, C., Liu, X. and Zhang, W. (2021) 'On the dispersion mechanism of the flutter boundary of the AGARD 445.6 Wing', *AIAA Journal*, Vol. 59, No 7, pp.2657–2669.

Gao, C., Zhang, W. and Ye, Z. (2016) 'A new viewpoint on the mechanism of transonic single-degree-of-freedom flutter', *Aerospace Science and Technology*, Mya, Vol. 52, pp.144–156, https://doi.org/10.1016/j.ast.2016.02.029.

Gao, C.Q., Zhang, W.W., Liu, Y.L., Ye, Z.Y. and Jiang, Y.W. (2015) 'Numerical study on the correlation of transonic single-degree-of-freedom flutter and buffet', *Science China: Physics, Mechanics and Astronomy*, Vol. 58, No. 8, Article Id. 084701.

Giannelis, N.F., Vio, G.A. and Levinski, O. (2017) 'A review of recent developments in the understanding of transonic shock buffet', *Progress in Aerospace Sciences*, July, Vol. 92, pp.39–84, https://doi.org/10.1016/j.paerosci.2017.05.004.

Hartmann A., Kallweit S., Feldhusen A. and Schröder W. (2012) 'Detection of upstream propagating sound waves at buffet flow using high-speed PIV', *Proceedings of the 16th International Symposium on Applications of Laser Techniques to Fluid Mechanics*, Lisbon, Portugal.

Iovnovich, M. and Raveh, D.E. (2015) 'Numerical study of shock buffet on three-dimensional wings', *AIAA Journal*, Vol. 53, No. 2, pp.449–463.

Lee, B.H.K. (2001) 'Self-sustained shock oscillations on airfoils at transonic speeds', *Progress in Aerospace Sciences*, Vol. 37, No. 2, pp.147–196.

Petrocchi A. and Barakos G. N. (2022) 'Buffet boundary prediction using RANS-based criteria and adjoint methods', *Aerospace Science and Technology*, Vol. 126, Article Id. 107664.

Plante, F., Laurendeau, E., Dandois, J. and Sartor, F. (2017) 'Study of three-dimensional transonic buffet on swept wings', *Proceedings of the 35th AIAA Applied Aerodynamics Conference*, Denver, Colorado, USA.

Sartor, F. and Timme, S. (2015) 'Reynolds–averaged Navier–stokes simulations of shock buffet on half wing–body', *Proceedings of the 53rd AIAA Aerospace Sciences Meeting*, Kissimmee, Florida, USA.

Sartor, F. and Timme, S. (2016) 'Mach number effects on buffeting flow on a half wing-body configuration', *International Journal of Numerical Methods for Heat and Fluid Flow*, Vol. 26, No. 7, pp.2066–2080.

Sartor, F. and Timme, S. (2017) 'Delayed detached–eddy simulation of shock buffet on half wing–body configuration', *AIAA Journal*, Vol. 55, No. 4, pp.1230–1240.

Timme, S. (2019) 'Global shock buffet instability on NASA common research model', *Proceedings of the AIAA SciTech Forum*, San Diego, California, USA.

Tinoco, E.N., Brodersen, O.P., Keye, S., Laflin, K.R., Feltrop, E., Vassberg, J.C., Mani, M., Rider, B., Wahls, R.A., Morrison, J.H., Hue, D., Roy, C.J., Mavriplis, D.J. and Murayama, M. (2018) 'Summary data from the sixth AIAA CFD drag prediction workshop: CRM cases', *Journal of Aircraft*, Vol. 55, No. 4, pp.1352–1379.

Vassberg, J.C., DeHaan, M.A., Rivers, S.M. and Wahls, R.A. (2008) 'Development of a common research model for applied CFD validation studies', *Proceedings of the 26th AIAA Applied Aerodynamics Conference, AIAA 2008-6919*, Honolulu, Hawaii, USA.

Xiao, Q.M., Tsai, H. and Liu, F. (2006) 'Numerical study of transonic buffet on a supercritical airfoil', *AIAA Journal*, Vol. 44, No. 3, pp.620–628.

Xiong, J., Liu, F. and Luo, S. (2012) 'Computation of NACA0012 airfoil transonic buffet phenomenon with unsteady Navier-Stokes equations', *Proceedings of the 50th AIAA Aerospace Sciences Meeting, AIAA 2012-0699*, Nashville, Tennessee, USA.

Zhang, W., Gao, C., Liu, Y., Ye, Z. and Jiang, Y. (2015) 'The interaction between flutter and buffet in transonic flow', *Nonlinear Dynamics*, Vol. 82, pp.1851–1865, https://doi.org/10.1007/s11071-015-2282-z.